STUDY OF NON-CONTACT ON-SITE SURFACE ROUGHNESS MEASUREMENT

STUDY OF NON-CONTACT ON-SITE SURFACE ROUGHNESS MEASUREMENT

By

HUIWEN JIA, B.Eng. (Electronic Engineering)

University of Electronic Science and Technology, Chengdu, Sichuan, China

A Thesis

Submitted to the School of Graduate Studies

in Partial Fulfillment of the Requirements

for the Degree

Master of Applied Science

McMaster University

MASTER OF APPLIED SCIENCE (2011) McMaster University

(Engineering Physics) Hamilton, Ontario

TITLE: Study Of Non-Contact On-Site Surface Roughness Measurement

AUTHOR: Huiwen Jia, B. Eng. (Electronic Engineering)

University of Electronic Science and Technology, China

SUPERVISOR: Dr. R. R. LaPierre

Department of Engineering Physics

McMaster University

NUMBER OF PAGES: LXXXVI, 86

Abstract

A non-contact on-site surface roughness measurement method was investigated in experimental and simulation approaches. The resolution of the vertical surface roughness was obtained at 20 nm by using self-interference theory. Various surface roughness measurement techniques, such as mechanical stylus, *AFM* and Michelson interferometer, were employed for different roughness samples. The novelty of this study was to measure the surface roughness on a rotating sample. For each sample with different step height, corresponding intensity distribution data was obtained and analyzed. The fringe visibility ratio resulted in a curve that is related to the step height, which represents the roughness. The results from simulations for all samples were compared with experimental data. Good agreements were obtained for the studied conditions.

Acknowledgements

I would like to first express my gratitude to my supervisor, Dr. R. R. LaPierre, for giving me a chance to complete this interesting study, and his instructive guidance and support throughout this research.

I would also like to heartfully thank Peter Jonasson for his invaluable assistance in conducting this research.

I would also like to thank Dr. Cassidy, Dr. Hesham and Dr. Ferdous for giving me thought provoking direction and advices.

I would also like to thank Doris, Zhilin Peng, Glen, Eugene, for the help in clean room operation and experimental instruments.

I would also like to thank my friends and colleagues, Abhi, Yi Gan, Fangfang Zhang, Qingyang Xu, for their help with experiment.

Finally, I would like to specially thank my husband, my daughters and my parents for their encouragement and support.

Contents

List of Figures

List of Tables

Nomenclature

a	Shifting space
A	Amplitude of oscillation
C_0	Fresnel cosine integral
C_1	Speckle contrast
d	Distance between two bright strips
dL_s	Flux of light scattering
h	Step height
	Surface profile at one point
I_0	dc intensity
I_1	Total intensity
I_d	Power of specular or reflection light
I_{in}	Power of incident light
I_L	Intensity at left side
$I_{L\text{-}normal}$	Normalized intensity at left side
I_{max}	Maximum intensity
I_{min}	Minim intensity
I_s	Power of scattered light
$I_{R\text{-}normal}$	Normalized intensity at right side
$J_1(z)$	First order Bessel function ($z = \frac{4p}{l} A$)
K	Co-efficient of system punctuation
k_1	Longitudinal wave number in the first media
l	Amplitude of surface contour
L_i	Total flux of incident light
n	Sampling number
r_l , r_r	Reflectivities of left and right sides

R_0	Total of specular reflection and scattering ratio
R_1, R_2	Two incident rays
Ra	Roughness average
R_{RMS}	Roughness root mean square
R_S	Specular reflectance ratio
S	Interference signal
	Illumination area
S_1	dc component of signal
S_0	Amplitude of ac component
	Fresnel sine integral
U	The amplitude of the wave at P point
V	Fringe visibility
z_i	Height between peak and valley

a_0	Phase difference of interference signal when mirror is still
a_r	Phase change of interference signal from measured surface profile
Dr	Path length difference between two rays
f	phase distribution
g	ac intensity
Ω_i	Solid angle of incident light
Ω_s	Solid angle of outgoing direction
q	Incident angle
q_i	Incident angle
r_0	Lateral correlation length
s	Root mean square surface roughness
l	Incident wavelength

w	Light frequency of (He-Ne laser)
w_0	Frequency of carrier
w_1	Side frequency
w_c	Angular frequency
w_m	Mechanical frequency in rotating

Chapter 1

Introduction

1.1 Background

Surface roughness measurement has been investigated over decades, ranging from millimeter to nanometer [1, 2, 3]. The measurement range larger than micrometer has been well developed in industry [4, 5, 6]. The roughness range smaller than the wavelength of incident light has been studied with reasonable applications as well. However, the instruments in market for the measurement on the nanometer range exhibit obvious disadvantages in the operation, for example, the instruments require stable and independent platform, not convenient for on-line measurement, which means the sample must be taken off the machine for measurement and reloaded for alignment from time to time [7, 8, 9]. Therefore, developing instruments for the on-line measurement is of industrial interest [10], since adjustments of manufacturing parameters may be determined based on the real time measurement without stopping the machining process or removing the work-piece. Also, the concepts involved in the measurement are broad and versatile, covering mathematical, mechanical, electrical and optical. In the following texts, various instruments with corresponding theories and applications are discussed, from the aspects of optical theories, laser source and instrument disadvantages.

The typical optical theories in surface roughness measurement include scattering method and interference method. The optical methods based on the scattering theory are only suitable for the roughness range that is far smaller than wavelength of the illuminating light [11, 12]. The fundamental limitation lies in the quarter wavelength [13, 14]. If the surface roughness is larger than the quarter wavelength, measurement with the scattering methods can only produce a range but not an exact value. The interference technique has an advantage for this application, i.e. the measurable roughness is close to or larger than a quarter of a wavelength, even though the interference method also has the problems of requiring stationary environment, complex optical setup and unsuitable for on-site measurement [15, 16].

The type of laser source is important to the measurement accuracy. The conventional laser source for measurement is a He-Ne laser at 632.8 nm. To carry out an accurate and quick in-situ measurement for the roughness ranging in 100-1000 nm is a problem for a single-wavelength laser source. A multi-wavelength technique using diode laser source for the distance measurement with resolution in the sub micrometer level was proven in the work of Enshasy and Cassidy [17]. This method incorporated multi-wavelength fringe counting and cosine fitting in data analysis, from which an accurate measurement result was obtained. Applied differently in the roughness measurement, the diode lasers with longer wavelengths can broaden the measurable range and increase the accuracy. However, if the roughness range is less than 100 nm, there is no

significant advantage by using multi and longer wavelengths. This will be further discussed in Chapter 5. A traditional He-Ne laser source with 632.8 nm was utilized as measuring roughness in nanometer range (less than 200 nm) is of interest in this study.

A typical instrument for surface roughness measurement is stylus profiler, which captures the peak and valley distribution of the surface once the size of the diamond tip is small enough compared to the lateral size of the surface irregularities. However, the disadvantages of stylus profilers include:

a). It can damage the surface being measured due to a direct contact;

b). It can only measure a limited length; and,

c). It only produces one-dimensional result of the surface.

Therefore, this research was aimed at developing a new optical method for the roughness measurement ranging (50-200 nm) for an accurate, non-contact, on-site measurement with simple setup.

1.2 Definition of surface roughness

The surface profile generally includes three effects: roughness, waviness, and form, as shown in Fig 1.1.

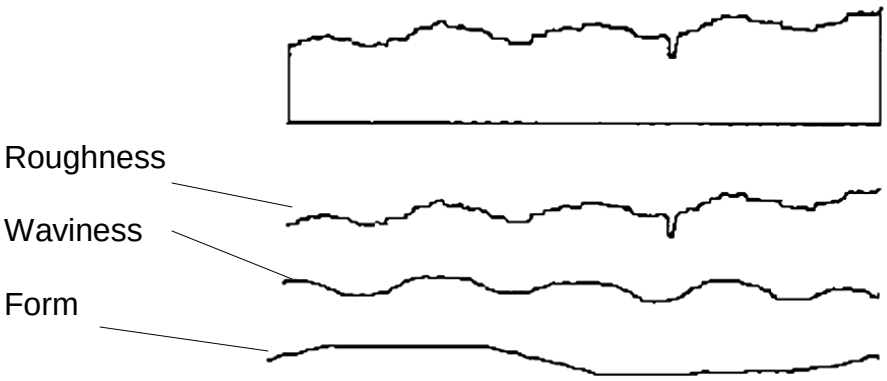

Figure 1.1 A surface profile with roughness, waviness, and form combined effects.

The small sinusoidal peak to valley profile is defined as surface roughness [18]. A machining process produces roughness due to tools, spark and grit. The roughness is sometimes regular, whereas it generally can be random due to different processes. A zoom in picture of surface roughness is shown in Fig. 1.2. The surface roughness is an important characteristic of surface quality and inevitable during the machining process. To describe a surface roughness, the peak values and valley values are required from the measurement. A given length is defined as roughness cutoff. If the asperity space is less than the roughness cutoff, the surface is considered as roughness; otherwise, it is considered as waviness. Waviness has more wide space and is not related to machining process. The main source of waviness is due to the unbalanced wheel or machine damping [19]. As shown in Fig. 1.1, waviness has a longer spatial wavelength than roughness. Form is the shape due to bending or deflection

when the work-piece is fixed on the machine. Heat treatment may bow a surface, which is considered as form errors.

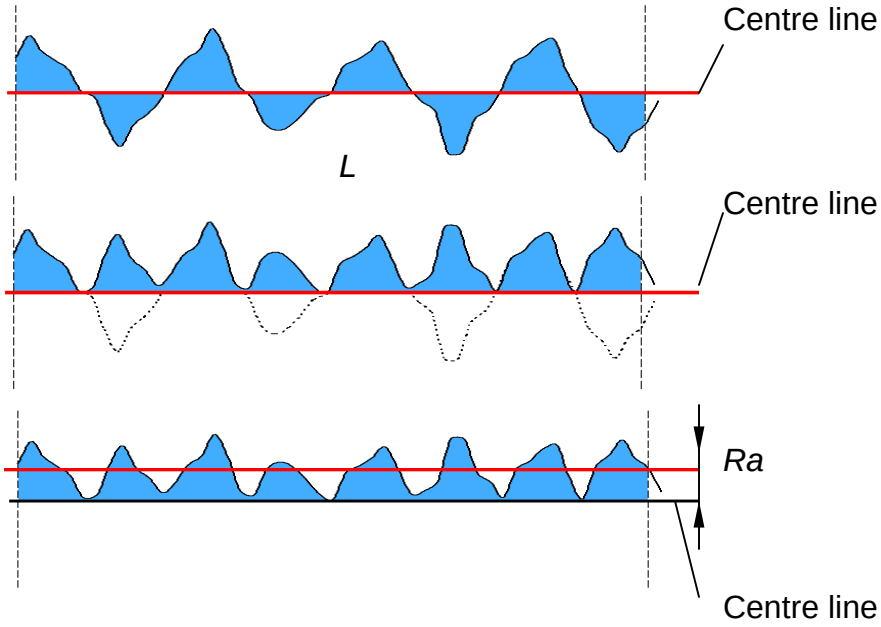

Figure 1.2 Definition graph of surface roughness *Ra*.

Fig. 1.2 shows the derivation of roughness average [19]. The portion below the centerline is interpolated. The expression for *Ra* [18, 20] is:

$$Ra = \frac{1}{n}\sum_{i=1}^{n} |z_i| \qquad \text{Eq. (1.1)}$$

where n and z_i are sampling number and the height between peak to valley in the range of the sampling length.

The *RMS* (root mean square) roughness was defined as [20]:

$$R_{RMS} = \sqrt{\frac{1}{n}\sum_{i=1}^{n} z_i^2} \qquad \text{Eq. (1.2)}$$

The above equation is suitable for a surface profiler, especially for a mechanical profiler [20]. A mechanical profiler obtains each point of the surface measured and output the surface coordinators at that point convolved with the stylus. The *RMS* value can then be calculated with Eq. (1.2).

1.3 Summary

Background and motivation of this research on the surface roughness measurement have been given in Chapter 1. As this work is mainly to develop an optical method of measurement, further mechanical issue regarding the surface roughness will not be discussed.

Methodology and experiment with results are given in the following chapters. Main theories and methods of surface roughness measurement are reviewed in Chapter 2. Calculation of typical case of surface roughness is provided in Chapter 3. Experimental setup and results are presented in Chapter 4. In Chapter 5, comparison of the difference between single wavelength laser source and multiwavelength laser source is provided, as well as suggestions for future work.

Chapter 2

Literature Review

In this study, in-situ surface roughness measurement was carried out without stopping the machine, or, a non-contact surface roughness measurement on a rotating sample. The related literatures are reviewed in the aspects of measurement methods (optical and mechanical), various optical theories (interference and scattering), and other measurement techniques.

2.1 Review of surface profiler

2.1.1 Comparison of optical and mechanical profiler

There are two types of surface profilers, namely mechanical profiler and optical profiler respectively [21]. Mechanical profilers collect data sequentially at slow speed and in contact with the surface of the specimen. For most situations, an optical profiler is chosen, due to the non-contact advantage. For comparison purpose, both mechanical profiler and optical profiler were employed in this work.

Mechanical stylus profiler obtains the step or height of the surface through the displacement of the stylus that is in contact with the surface. The measured data was digitalized through a computer [22]. The shortage of this method is that the tip of the stylus is easy to scratch due to direct contact. The stylus could damage the surface of the sample, which influences the measurement. The

measurement must be carried out in a clean and stable condition. Also, the measurement range is very limited because it can only provide two-dimensional surface maps. Due to these limitations, mechanical profiler is not suited for the on-line or in-process measurement.

2.1.2 Review of interferometer

Optical method includes optical profiler and parametric techniques [23]. The most common optical profiler is an interferometer. Interferometer can produce a map of the surface roughness point by point along the surface. The surface topography is calculated from the digital or analog signal, which is acquired from the interferometer. There are other kinds of optical profilers such as a transducer profiler. The main component is a microscope objective, which obtains information from two photo detectors. The transducer can provide one-dimensional surface profile [24]. This type of profiler has 10 *μm* lateral resolution and 0.1 *μm* vertical resolution. Optical profilers have many advantages: non-contact, fast parallel data acquisition, linear and area array.

Recent work for surface roughness measurement is related with a phase shifting technique [25][26]. The basic equations for the intensity of the two beams interference are given:

$$I_1(x,y) = I_0(x,y) + g\ (x,y)\cos\{(j\ (x,y))\} \qquad \text{Eq. (2.1)}$$

$$I_2(x,y) = I_0(x,y) + g\ (x,y)\cos\left\{\left(j\ (x,y) + \frac{p}{2}\right)\right\} \qquad \text{Eq. (2.2)}$$

$$I_3(x,y) = I_0(x,y) + g\ (x,y)\cos\{(j\ (x,y) + p)\} \quad \text{Eq. (2.3)}$$

$$I_4(x,y) = I_0(x,y) + g\ (x,y)\cos\left\{\left(j\ (x,y) + \frac{3p}{2}\right)\right\} \quad \text{Eq. (2.4)}$$

where, I_0 is a dc intensity,

$g\ (x,y)$ is an ac intensity,

$f(x,y)$ is a phase distribution.

By recording the above four step intensity images, the phase distribution can be calculated:

$$f(x,y) = \arctan\left[\frac{I_4(x,y) - I_2(x,y)}{I_1(x,y) - I_3(x,y)}\right] \quad \text{Eq. (2.5)}$$

The phase distribution can be translated into a surface contour:

$$f(x,y) = \frac{4p}{l} z(x,y) \quad \text{Eq. (2.6)}$$

The main problem of phase shifting interferometer includes [26]:

a). Sensitivity to mechanical vibration;

b). Nonlinear ramp motion;

c). Detector noise;

d). Environmental error sources: external vibration, acoustic noise, airflow turbulence, and temperature change during measuring.

Phase shifting interferometer has some faults such as inaccurate phase shifting, strong noise, low resistance to environmental disturbance and complex structure.

To perform a real time measurement, sinusoidal phase modulating interferometer was reported [27]. The main procedure to obtain surface profile is summarized below:

The signal generated from a Piezo Transducer is sinusoidal modulated as:

$$V(t) = A\cos(w_c t) \qquad \text{Eq. (2.7)}$$

where *A* is the amplitude of the oscillation,

w_c is the angular frequency.

Interference occurs between the sample and the oscillated mirror. The inference signal can be expressed as:

$$S(x, y, t) = S_1(x, y) + S_0(x, y)\cos((A\cos(w_c t) + a_0 + a_r(x, y))) \qquad \text{Eq. (2.8)}$$

where S_1 is dc component of the signal,

S_0 is the amplitude of the ac component,

a_0 is the phase difference of the interference signal when the mirror is still.

$a_r(x, y)$ is the phase change of the interference signal arising from the measured surface profile *r(x, y)*:

$$a_r(x, y) = \frac{4p}{l_0} r(x, y) \qquad \text{Eq. (2.9)}$$

Ignoring the dc component, after phase demodulation and filtering [28], the signal can be:

$$P(x, y) = KJ_1(z)\sin(a(x, y)) \qquad \text{Eq. (2.10)}$$

where *K* is a co-efficient of the system punctuation,

$J_1(z)$ is the first order Bessel function ($z = \frac{4p}{l} A$),

With $a(x,y) = a_0 + a_r \approx \frac{P(x,y)}{K}$, the final surface profile can be obtained as

$$r(x,y) = a(x,y)\frac{l}{4p} \qquad \text{Eq. (2.11)}$$

Although the advantage of the sinusoidal phase modulation technique has high accuracy and resistance to disturbance, this method received little notice.

The above methods, mainly phase modulation and sinusoidal phase modulation, are all based on interference theory, which have been well developed. This research incorporates both the theories of interference and scattering, which has not been reported. In the following texts, the literature of scattering method will be reviewed.

2.1.3 Scattering method for surface roughness measurement

Total integrated scattering (*TIS*) and Angle resolved scattering (*ARS*) are the main techniques for surface roughness measurement. Scattering methods normally give a quantitive result of a specific surface. Equations for weak scattering from a surface was derived [29]. The final simplified equation related to the surface roughness is shown below.

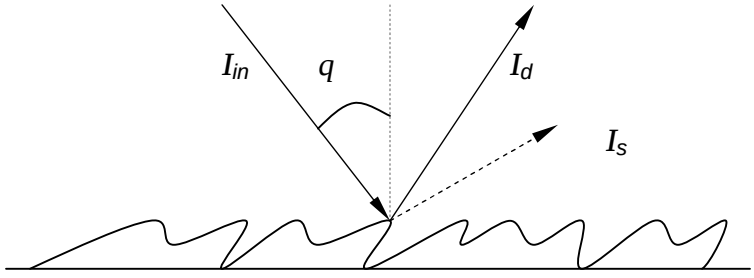

Figure 2.1 Scattering from a rough surface.

$$I_{in} = I_s + I_d \qquad \text{Eq. (2.12)}$$

$$C_1 = \frac{\sqrt{1 + 2\left(I_s / I_d\right)}}{1 + I_s / I_d} \qquad \text{Eq. (2.13)}$$

$$s = \frac{l}{4p\cos q r_0}\sqrt{\frac{S}{2p}\left[\frac{1}{\sqrt{1 - C_1^2}} - 1\right]} \qquad \text{Eq. (2.14)}$$

where s is the root mean square roughness,

r_0 is the lateral correlation length,

C_1 is the speckle contrast,

q is the incident angle,

l is the incident wavelength,

S is the illumination area,

I_{in} is the power of the incident light,

I_s is the power of the scattered light,

I_d is the power of the specular or reflection light.

The *TIS* method was further developed by using specular and scattering part of laser light from the surface that is being measured [29, 30].

$$TIS = 1 - \frac{R_s}{R_o} = 1 - \exp\left[-\left(\frac{4ps\cos q_i}{l}\right)^2\right] \qquad \text{Eq. (2.15)}$$

where R_s is the specular reflectance ratio,

R_0 is the total of the specular reflection and scattering ratio,

q_i is the incident angle,

l is the wavelength of the incident laser beam,

s is the *RMS* surface roughness.

By measuring the specular reflectance and total reflection, the *TIS* value can be calculated. Incorporating Eq. (2.15), the root mean square s can be calculated. Based on Bechmann and Spizzichino's scattering model for rough surface with roughness much smaller than the wavelength of the incident light (<<*λ/4*), another method to achieve *TIS* is angular resolved scattering (*ARS*) method [31].

$$BRDF = \frac{dL_s(\Omega_s)}{L_i \cos q_i d\Omega_i} \qquad \text{Eq. (2.16)}$$

where dL_s is the flux of light scattering,

L_i is the total flux of incident light,

Ω_i is the solid angle of the incident light,

Ω_s is the solid angle of outgoing direction.

In the above equation, bi-directional reflectance distribution function (*BRDF*) can be measured directly (details in reference [31, 32, 33]).

The *ARS* can be obtained as:

$$ARS = BRDF \cos q_s \qquad \text{Eq. (2.17)}$$

Thus, *TIS* is the integral of the *BRDF*:

$$TIS = \int BRDF \cos q_s d\Omega_s = \int_0^{p/2} \sin q_s dq_s \int_0^{2p} BRDF \cos q_s df_s \qquad \text{Eq. (2.18)}$$

The parameters q_i, q_s and f_s are indicated in Fig. 2.2.

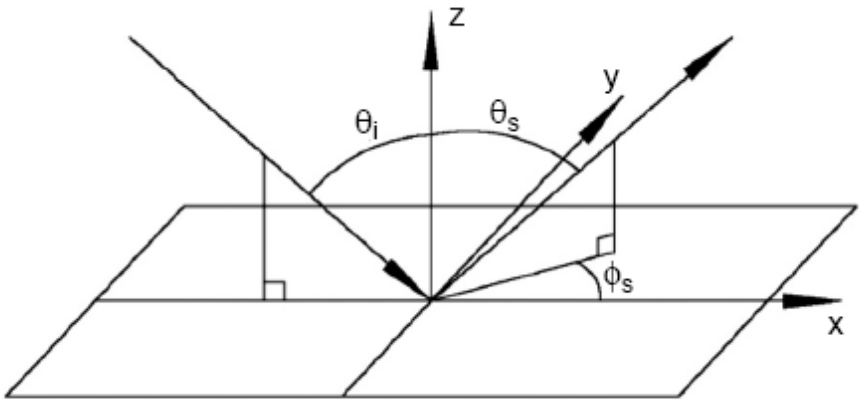

Figure 2.2 The geometry angle used in Eq. (2.18) [31].

TIS and *ARS* are typical roughness measurement instruments, which are already commercially available. However, sometimes when no diffuse reflection is observed, there are still some parts of the light beside reflection absorbed by the material. Also, some of light might transmit through the material. The optical

method cannot overcome those problems, which affects the measurement accuracy. This is the motive that other non-optical techniques were investigated.

2.1.4 Other literatures about surface roughness measurement

Other non-contact measurement techniques include capacitor and inductor techniques, thermal comparison, and pneumatic gauges [34].

One modified reflection coefficient [35] for Gaussian distribution of surface roughness can be expressed as

$$R = R_0 e^{-2h^2 k_1^2} \qquad \text{Eq. (2.19)}$$

where, k_1 is longitudinal wave number in the first media,

h is surface profile at one point (x, y).

Phase modulation by surface roughness can be written as

$$f(x, y) = -2h(x, y)k_1 \qquad \text{Eq. (2.20)}$$

According to the Kirchhoff approximation and small amplitude phase perturbation, the surface profile can be considered as an ergodic random process. The probability density distribution $p(f)$ has the relationship with electrical field [36]:

$$E = E_0 \int_{-\infty}^{\infty} e^{if} p(f) df \qquad \text{Eq. (2.21)}$$

Whitefield measured a surface profile using an optical Fourier transform technique [36]. Goedgebuer *et al*. developed a temporal holography profiler that uses holography, spectroscopy and interferometry [37]. However, the last two

profilers have not been examined by industry [38]. Especially the last one is still in the experimental stage.

2.2 Summary

Different surface profilers (non-contact and contact) and various theories have been reviewed in this chapter. To most optical instruments for roughness less than 100 nm, the measurement techniques are limited to very small roughness value which is far smaller than incident wavelength, although these instruments demonstrates advantages and disadvantages in various aspects. No research employing a rotating sample for roughness measurement has been reported.

The novelty of this research is that currently no work of non-contact on-site measurement on a rotating sample with roughness close to 50 nm has been reported. The detail methodology will be presented in the next chapter.

Chapter 3

Theory

Optical interference and scattering theory have been commonly employed in industry. However, the applications are limited in roughness measurement far smaller than incident wavelength. To analyze a 30-600 nm or rougher surface, interference and scattering methods will have difficulties: fringe ambiguity for interference and theoretical assumption are not valid for scattering. Therefore, multi-wavelength to overcome the fringe ambiguity for interference technique, and self-interference to solve the problem from scattering theory, are the main tasks for future work. In this research, measurement on surface roughness around 30-100 nm is of interest. The theory is concentrated on self-interference. Further discussion regarding multi-wavelength technique will be provided in Chapter 5.

3.1 Self-interference theory

Self-interference method is a kind of interferometry, which combines scattering and interference. Once the light hits at a step area, scattering and interference happen at the same time. With different step height, the reflected

light will have different bright and dark ratio. Those bright and dark strips compose self-interference fringes.

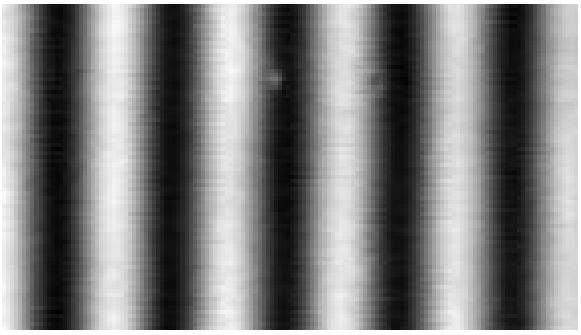

Figure 3.1 Self-interference fringes.

To analyze the fringes due to self-interference in Fig. 3.1, a fundamental example is a step with rectangular shape.

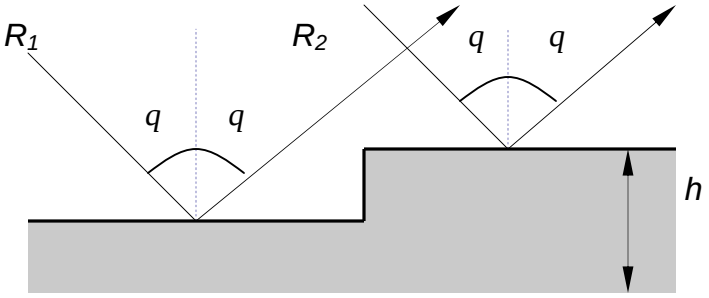

Figure 3.2 Diagram of optical path between two rays.

In Fig. 3.2, the path length difference between the two rays is:

$$\Delta r = 2h\cos q \qquad \text{Eq. (3.1)}$$

where q is the incident angle,

R_1 and R_2 are two incident rays,

h is the step height.

The phase difference can be express as:

$$\Delta f = 2p\Delta r / l = 4ph\cos q / l \qquad \text{Eq. (3.2)}$$

It is to be noted that if the phase difference is $\Delta f = p$, modulo $2p$, there will be destructive interference [39]. The approximate unambiguous measurement range is:

$$h < \frac{l}{4\cos q} \qquad \text{Eq. (3.3)}$$

From the above equation, if l is 632.8 nm, nanometer range (100-300 nm) rough surface will challenge Eq. (3.3). Some data may be out of range. Extending the wavelength to an IR (1550 nm) laser source, or, using the multiple wavelengths can solve this problem.

In this work, the test range was focused on nanometer (30-100 nm). The fringe visibility method will be introduced in the following section.

3.1.1 Derivation of intensity distribution for a simple rough surface

In Fig. 3.3, the incident beam covers the step area and produces division of wavefront after meeting the step. The reflected beams interfere and a fringe can be observed. To analyze the simple model [40], a cylindrical coordinate system is introduced.

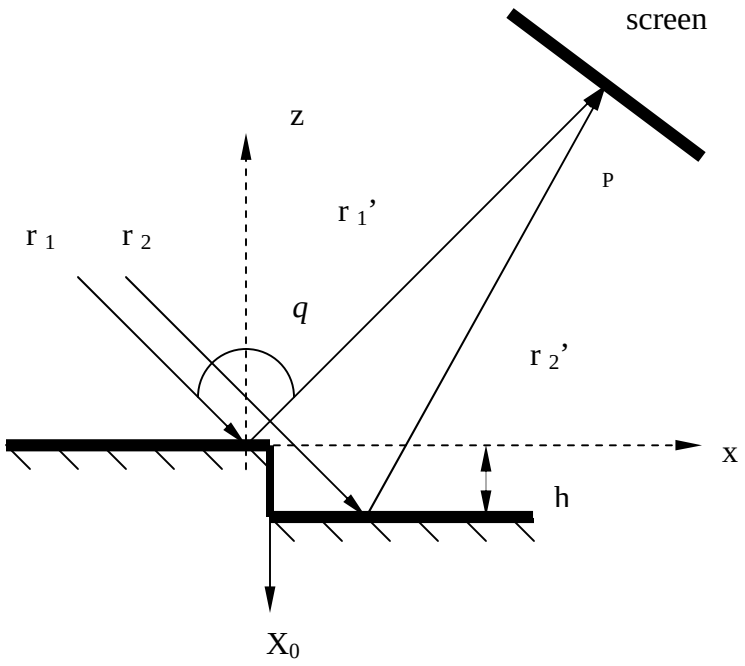

Figure 3.3 Geometry of the calculation of Fresnel – Kirchhoff integral.

Fresnel-Kirchhoff integral expression [40] is shown below:

$$U(P) = A\left[r_1 \int_{-\infty}^{x_0} \frac{e^{ik(r_1 + r'_1)}}{\sqrt{r_1 r'_1}} dx_1 + r_2 \int_{x_0}^{+\infty} \frac{e^{ik(r_2 + r'_2)}}{\sqrt{r_2 r'_2}} dx_2 \right] \qquad \text{Eq. (3.4)}$$

Ignore small terms and Fresnel approximation [40], Eq. (3.4) can be expressed as:

$$U(P) = A\left[r_1 \int_{-\infty}^{x_0} e^{\frac{ipx^2}{2}} dx + e^{if} r_2 \int_{x_0}^{+\infty} e^{\frac{ipx^2}{2}} dx \right] \qquad \text{Eq. (3.5)}$$

Because the integrands are even and $\int_0^{+\infty} e^{\frac{ipx^2}{2}} dx = \frac{1}{2}(1+i) = (C_0 + iS_0)$ [41]

The Eq. (3.5) can be re-written as:

$$U_1(P) = A\left[\frac{1}{2}(1+i)\left(r_l + r_r e^{if}\right) + \left(C_0 + iS_0\right)\left(r_l - r_r e^{if}\right)\right] \qquad \text{Eq. (3.6)}$$

After multiply its complex conjugate $U_1^*(P)$,

$$I_1 = I_0 r_l r_r\left[\frac{1}{2}\cos f - \left(C_0 - S_0\right)\sin f - \left(C_0^2 + S_0^2\right)\cos f\right] + \frac{I_0}{2}\left[\left(\frac{1}{2} + C_0^2 + S_0^2\right)\left(r_l^2 + r_r^2\right) + \left(C_0 + S_0\right)\left(r_l^2 - r_r^2\right)\right] \qquad \text{Eq. (3.7)}$$

where, $I_0 = U^* U$,

$f = 4ph\cos q / l$,

C_0 is the Fresnel cosine integral [40],

S_0 is the Fresnel sine integral,

r_l and r_r are reflectivities of the left and the right side.

For an ideal optical metal surface case, $r_l = r_r = 1$, Eq. (3.7) can be simplified as:

$$I_L = I_0\left[\cos^2\left(j/2\right) + 2\left(C_0^2 + S_0^2\right)\sin^2\left(\frac{j}{2}\right) - \left(C_0 - S_0\right)\sin j\right] \qquad \text{Eq. (3.8)}$$

The normalized expression is:

$$I_{Lnormal} = \cos^2\left(j/2\right) + 2\left(C_0^2 + S_0^2\right)\sin^2\left(\frac{j}{2}\right) - \left(C_0 - S_0\right)\sin j \qquad \text{Eq. (3.9)}$$

$$I_{Rnormal} = \cos^2\left(j/2\right) + 2\left(C_0^2 + S_0^2\right)\sin^2\left(\frac{j}{2}\right) + \left(C_0 - S_0\right)\sin j \qquad \text{Eq. (3.10)}$$

Equation (3.9) and (3.10) are the intensity distribution for left side and right side of the step. From the equations, the intensity distribution is periodic per $l/2$.

In total, the intensity for observation position *P* from the left to right side can be expressed as (details in reference [40]):

$$I_{normal} = \cos^2(f/2) + 2\left(C_0^2 + S_0^2\right)\sin^2\left(\frac{f}{2}\right) + \left(C_0 - S_0\right)\sin f \qquad \text{Eq. (3.11)}$$

The calculation result is show below:

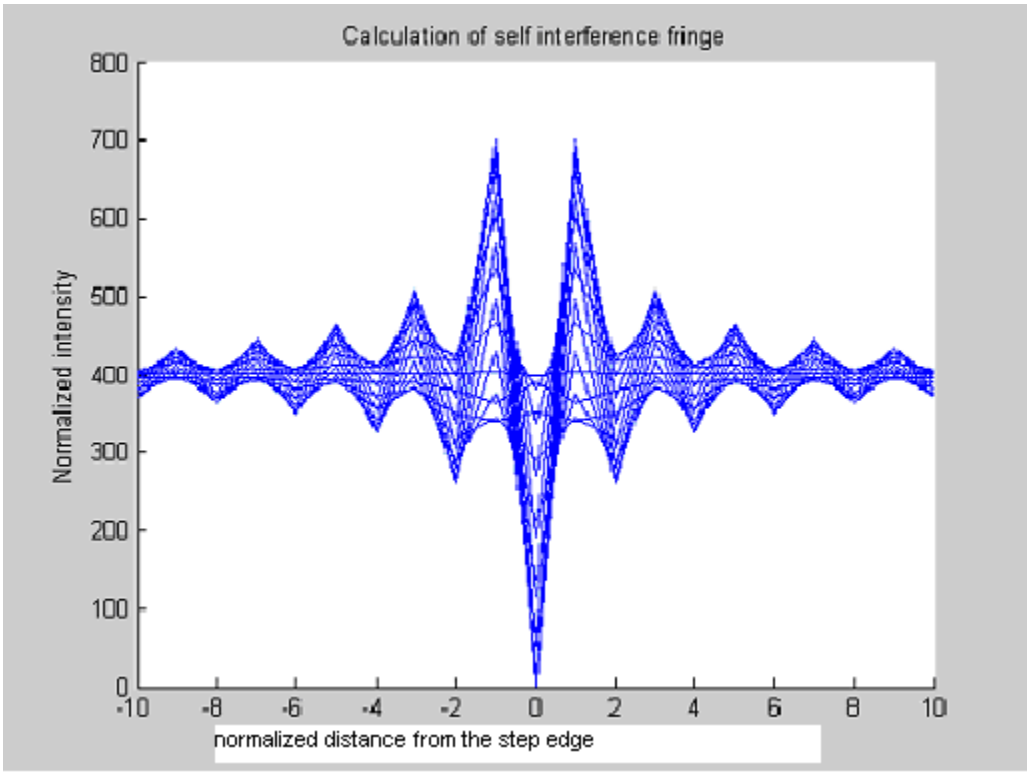

Figure 3.4 Calculation of Self-interference fringe.

By substituting the maximum and minimum intensities into the Eq. (3.12), the fringe visibility is calculated as Fig. 3.5.

$$V = \frac{I_{\max} - I_{\min}}{I_{\max} + I_{\min}} \qquad \text{Eq. (3.12)}$$

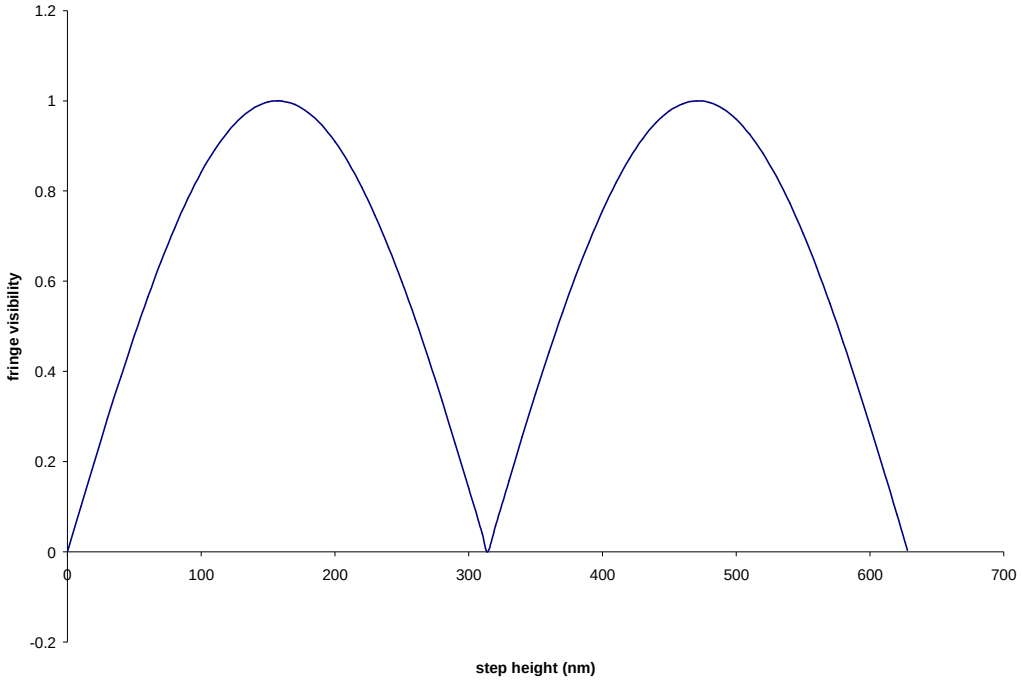

Figure 3.5 Fringe visibility to surface step height (l is 632.8nm).

In Fig. 3.5, the fringe visibility will reach maximum value when step height is equal to quarter wavelength. The fringe visibility has the relationship with step height as [40]:

$$Fringe\_visibility \propto \left|\sin\Phi\right| = \left|\sin\left(h\cos q\right)\right| \qquad \text{Eq. (3.13)}$$

where *h* is the height of the step,

q is the incident angle.

Fringe visibility is proportional to an absolute value of a sinusoidal function. For example, when $h = \frac{l}{4}$, and incident angle $q \approx 0$, then fringe visibility is unity.

As shown in Fig. 3.6, by increasing the incident angle q, the calculation shows that the fringe visibility value decreases certain amount at the same step height sample, and then at larger step height the fringe visibility will reach unity.

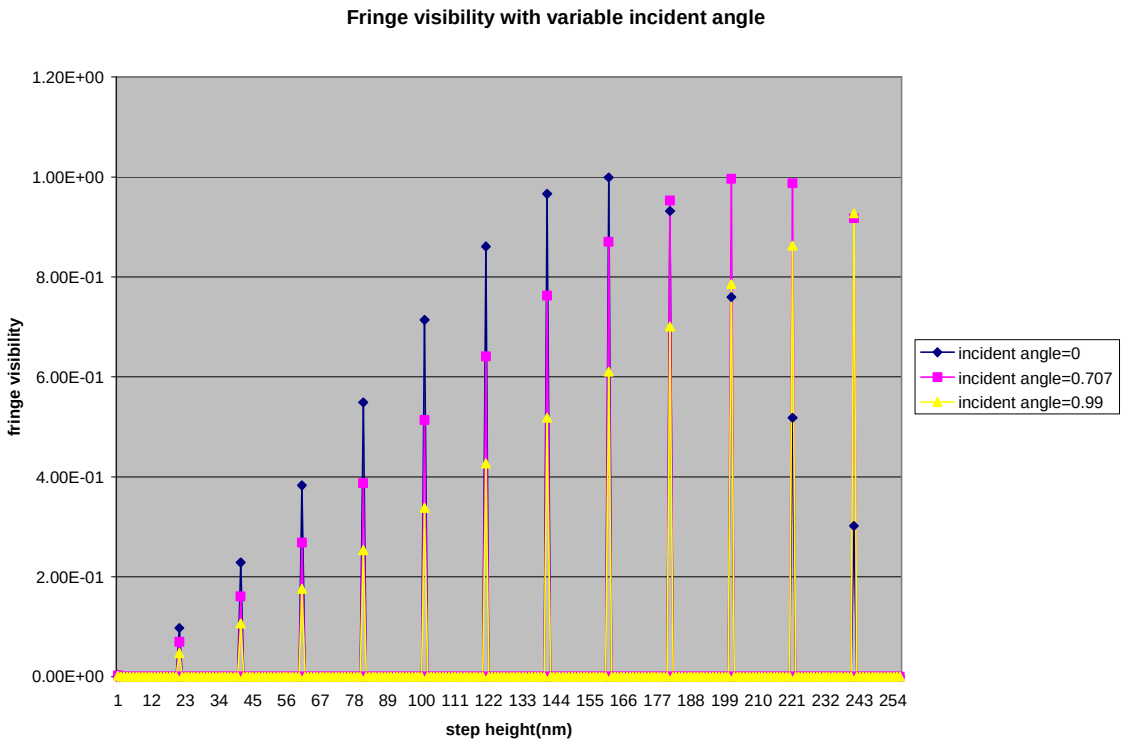

Figure 3.6 Fringe visibilities with variable incident angle.

In this research, only the calculation for changing the incident angle is provided.

The conclusion for fringe visibility of self-interference is that fringe visibility will decrease to zero when the step height is close to zero. The maximum value of the fringe visibility (unity) happens when the step height is equal to $l/4$. The method of fringe visibility method has some advantages:

a). it is not influenced by environmental condition (air flow, temperature, pressure, vibrations);

b). it needs a simple setup, but other optical interference measurement, such as phase modulation interferometer, white light heterodyne interferometer, need complicated setup with many optical elements.

3.1.2 Power spectrum density of signal measured from rough surface

This study is to explore a method to measure surface roughness with rotating sample. When the sample is rotating, the incident light is modulated. The feedback beam carrying self-interference information is analyzed by calculating the power spectrum density (*PSD*).

In the calculation of self-interference, if the step is higher, the amplitude of the signal will be accordingly larger. Ideally, if there is no mechanical influence, the feedback light can produce a pulse train signal when the sample is rotating. Each pulse is related to each step. Steps are different, and the amplitude of the pulse is also different. This is similar to the rough surface. The analysis with communication theory on the signals was applied differently on this subject.

Based on the communication theory, the signal at the detector was analyzed in order to describe a phase modulated incident beam through a rotating polarizer [42]. By using polar coordinates (r,q) for the specimen, the amplitude of the wave is obtained as $r_k^2 m(r,q)$ over an area $drrdq$ for each plane

wave k. Assuming the phase of the electric field of the illumination is $j(k,l)$. Because the specimen is rotating at a mechanical frequency of w_m, Eq. (3.14) was derived from reference [42]:

$$P=\left\langle \overline{m'(r,q)^2}\cos^2(wt+kl)\right\rangle+\left\langle 2\overline{m'(r,q)}\cos(wt+kl)\times\overline{r(r,q)\times m(r,q)\cos[wt+kl(r,q)]}\right\rangle +\left\langle \overline{r(r,q)\times m(r,q)\cos[wt+kl(r,q)]^2}\right\rangle \quad \text{Eq. (3.14)}$$

The term of $\cos[wt+kl(r,q)]$ is the phase modulation part, which can be expanded in a Fourier series. l represents h in Fig. 3.2. By using the communication theory for phase modulation [43], the signal at the detector can be summarized as:

$$E(t)=\cos[wt+\sum_{i=1}^{k} z\sin(iw_m t)] \quad \text{Eq. (3.15)}$$

where $\sum_{i=1}^{k} z\sin(iw_m t)$ is the Fourier series of a periodical signal when the sample is rotating.

To expand the signal, the Jacobi-Anger relations can be used to get the harmonics [42], which can be simplified as the following formula:

$$E(t)=\sum_{-\infty}^{+\infty} J_n(z)\cos[(w+nw_m)t] \quad \text{Eq. (3.16)}$$

where $z=2kl=2\times\frac{2p}{l}\times l$,

l is the amplitude of the surface contour (*l* is the same as *h* in Fig 3.2),

w is light (He-Ne laser) frequency (high),

w_m is the mechanical rotating frequency (low),

The detail derivation of Eq. 3.16 is shown below:

One *RF* signal can be written as:

$$a = A\cos f \qquad \text{Eq. (3.17)}$$

where, A is the amplitude of the signal, $w = {df}/{dt}$ is the angular velocity. Only frequency / phase modulation will be expressed here.

For mathematical way, one signal is frequency/phase modulated by one specific sinusoidal wave can be written as:

$$w = w_0(1+ f(t)) = w_0(1 + c_0 + \sum_{i=1}^{k} c_i \cos(w_i t + q_i)) \qquad \text{Eq. (3.18)}$$

$$f = \int w dt = w_0(t + \int f(t)dt) = w_0(1+c_0)t + \sum_{i=1}^{k} \frac{c_i w_0}{w_i} \cos(w_i t + q_i)) \qquad \text{Eq. (3.19)}$$

Substitute Eq. (3.18) into Eq. (3.19), then

$$a = A_0 \cos\left[w_0(1+c_0)t + \sum_{i=1}^{k} z_i \cos(w_i t + q_i) \right] \qquad \text{Eq. (3.20)}$$

where, $z_i = \frac{c_i w_0}{w_i}$.

For pure frequency modulation, c_i is a constant. For phase modulation, c_i is a product of a constant by f_i.

Assuming *i* = 1, Eq. (3.20) is

$$a = A_0 \cos[w_0(1+c_0)t + z_1 \cos(w_1 t + q_1)] \qquad \text{Eq. (3.21)}$$

where w_0 is carrier frequency

w_1 is side frequency.

By expanding Eq. (3.21),

$$a = A_0\left[\cos\{w_0(1+c_0)t\}\cos\{z_1\cos(w_1t+q_1)\} - \sin\{w_0(1+c_0)t\}\sin\{z_1\cos(w_1t+q_1)\}\right]$$

Eq. (3.22)

Jacobi-Anger relations [43] are:

$$\cos(y\cos x) = \sum_{n=-\infty}^{\infty}(-1)^n J_{2n}(y)\cos(2nx)$$ Eq. (3.23)

$$\sin(y\sin x) = \sum_{n=-\infty}^{\infty} J_{2n-1}(y)\sin((2n-1)x)$$ Eq. (3.24)

Substituting Eq. (3.23) and Eq. (3.24) into Eq. (3.22),

$$a = A_0\left[\cos\{w_0(1+c_0)t\}\sum_{n=-\infty}^{\infty}J_{2n}(z_1)\cos 2n(w_1t+q_1) - \sin\{w_0(1+c_0)t\}\sum_{n=-\infty}^{\infty}J_{2n-1}(z_1)\sin(2n-1)(w_1t+q_1)\right]$$

Eq. (3.25)

Using trigonometric identities in (3.25)

$$a = \frac{A_0}{2}\sum_{n=-\infty}^{\infty}[J_{2n}(z_1)(\cos[w_0(1+c_0)t + 2n(w_1t+q_1)] + \cos[w_0(1+c_0)t - 2n(w_1t+q_1)])$$
$$+ J_{2n-1}(z_1)(\cos[w_0(1+c_0)t + (2n-1)(w_1t+q_1)] - \cos[w_0(1+c_0)t - (2n-1)(w_1t+q_1)])]$$

Eq. (3.26)

Base on Eq. (3.26), a code was developed for simulating power spectrum density of the signal (Appendix A). In the simulation, if the height of the step is low (close to 10 nm), the fringe contrast ratio is small. Accordingly, the amplitude of the pulse signal from the detector is small, whereas the first order harmonic will be higher than other harmonics. On the contrary, if the height of the step is

high (close to 70 nm), the fringe contrast ratio is larger. The amplitude of the pulse signal from the detector is larger, whereas the first order harmonic will be lower and second order harmonic will be stronger. The trends can be found in Fig. 3.7.

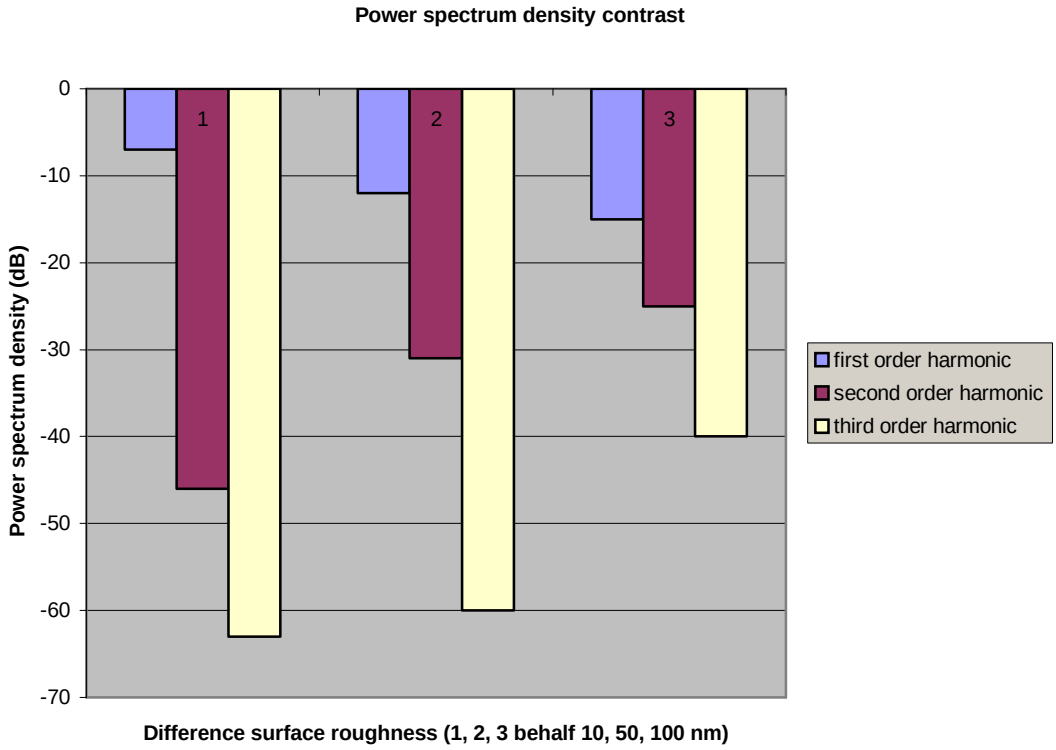

Figure 3.7 Comparison of *PSD* trends for difference rough samples.

An example with 200 nm step height is given in Fig. 3.8.

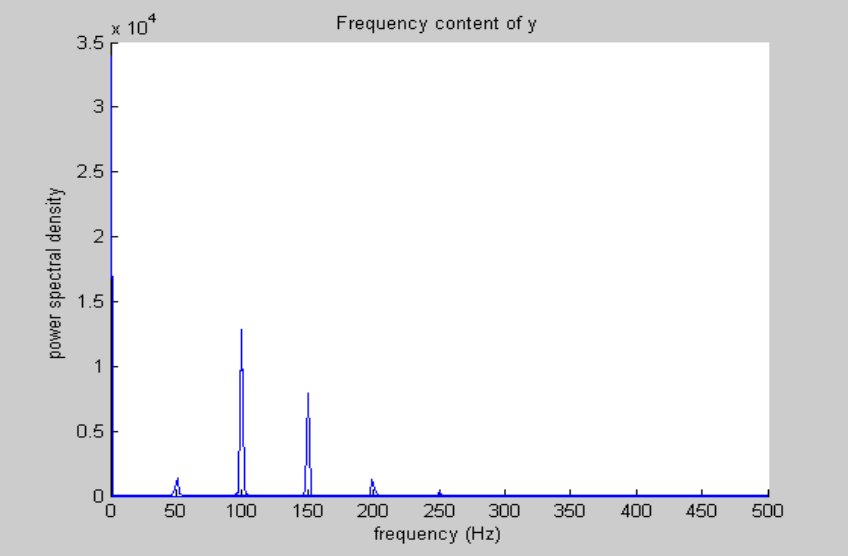

Figure 3.8 Calculation of *PSD* for 200 nm step height sample.

From the above figure, the first order harmonic is obviously lower than the second order harmonic. The reason to calculate the *PSD* is to find if the *PSD* method can be adapted into surface roughness, If the harmonics from the measurement have the same trends with the simulation, further surface roughness investigation will be necessary by measuring the *PSD* value of the signal from the detector.

Theoretically, the total amplitudes of the base band harmonics (ignoring small terms) are related to RMS roughness of the rough surface. As the sample is rotating, the feedback beam always forms a circle. The detector catches all the feedback light, thus the signal makes no difference. By decreasing the size of the detector, the signal may show an intensity modulation carrying small peaks related with steps. Since the electrical power spectral density measurement from spectral analyzer is sensitive and changes randomly, there is no obvious

difference between the data related to the difference step heights. However, if keeping the sample not rotating, the power spectrum density does show the difference, which will be presented in Chapter 4. The improvement for this self-interference method in the future work is to introduce a *CCD* image camera.

3.2 Summary

Based on the analysis and derivations, a new interesting technique combining fringe visibility measurement and power spectrum density measurement is a novel method to obtain roughness in a range of 30-300 nm. Detail measurement results and comparisons of Michelson interferometer and self-interference (fringe visibility and *PSD*) will be provided in Chapter 4. The problems for each method will be discussed as well.

Chapter 4

Experiments and Results

In this Chapter, samples with various step heights are measured in different setups for different theories. Test results are compared and discussed. The setups include Michelson interferometer [44, 45] (with rotating sample, and with stationary sample), self-interferometer with rotating sample. For comparison purpose, other non-optical measurement techniques, such as atomic force microscopy (*AFM*) [46] and mechanical stylus (a step) are employed in the experiment as well.

4.1 Sample preparation

The roughness is simplified as regular pattern, or, rectangular steps with different heights, on a Silicon wafer (Fig. 4.1). The wafer is rinsed with HF solution for oxide layer deposition on the top. With UV exposure for photo resist and SiO_2 layer etching, aluminum thin film with different heights are deposited onto the designated areas, as shown in Fig. 4.2. Details of sample preparation are given in Appendix D.

In Fig. 4.2, the black area is a step (rough area) and white area is flat (smooth area). Currently, only one style sample, which has same height in the

steps in one wafer, was processed. For future work, one sample with different height in steps can be processed for comparison.

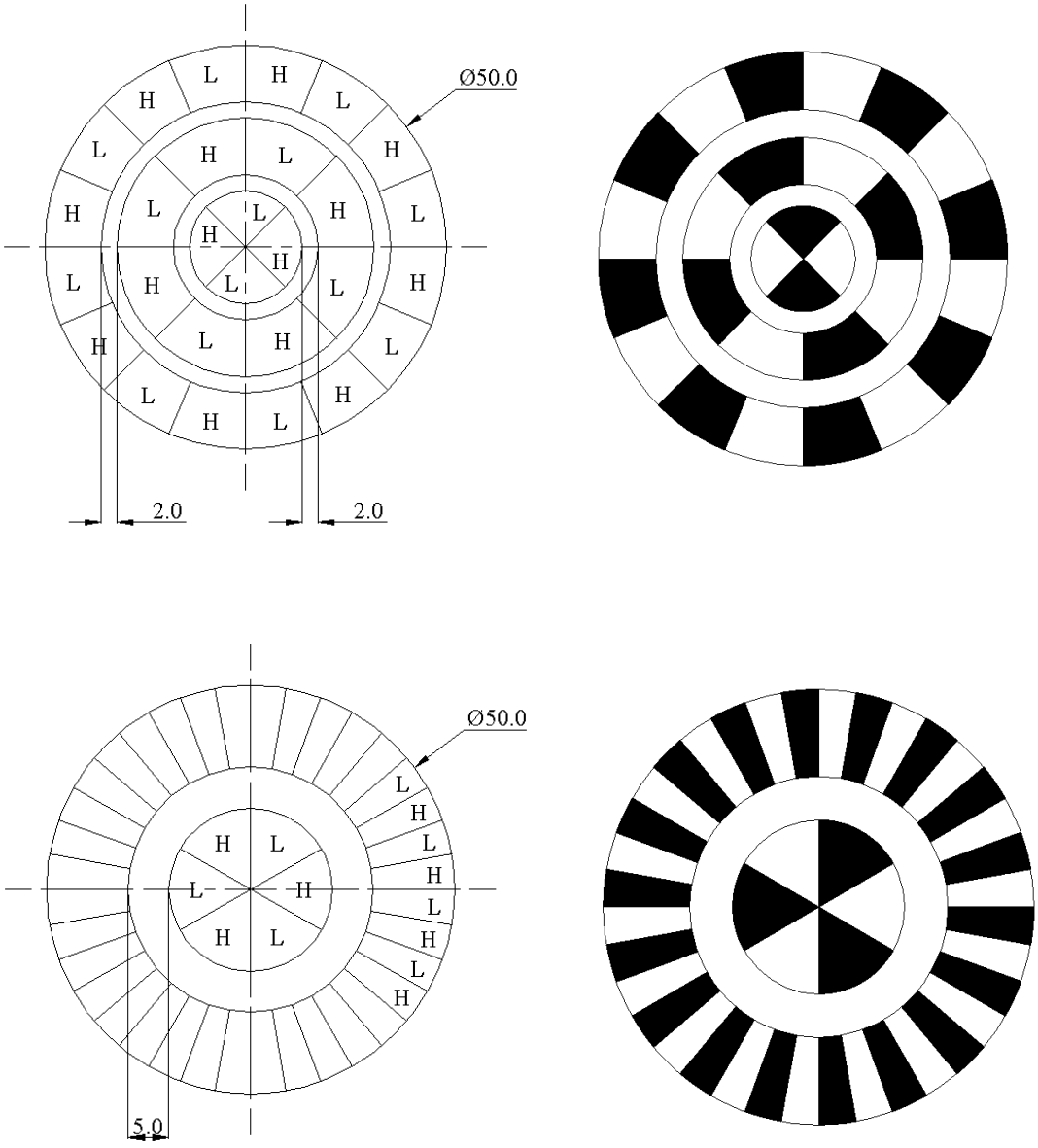

Figure 4.1 Sample patterns for 2 inch Wafer (unit of dimensions in figures is mm).

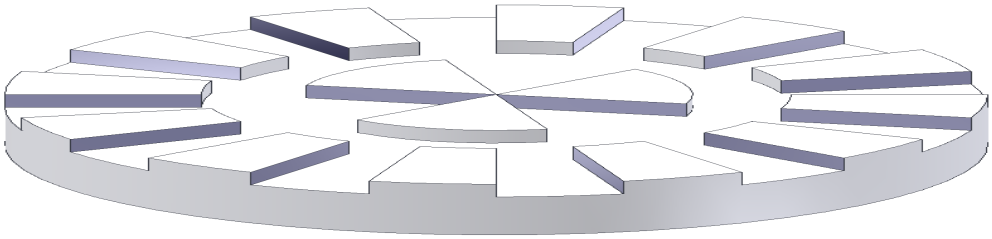

Figure 4.2 3D Aluminum surface sample with steps.

4.2 Experiments and measurement results

4.2.1 Self interference measurement

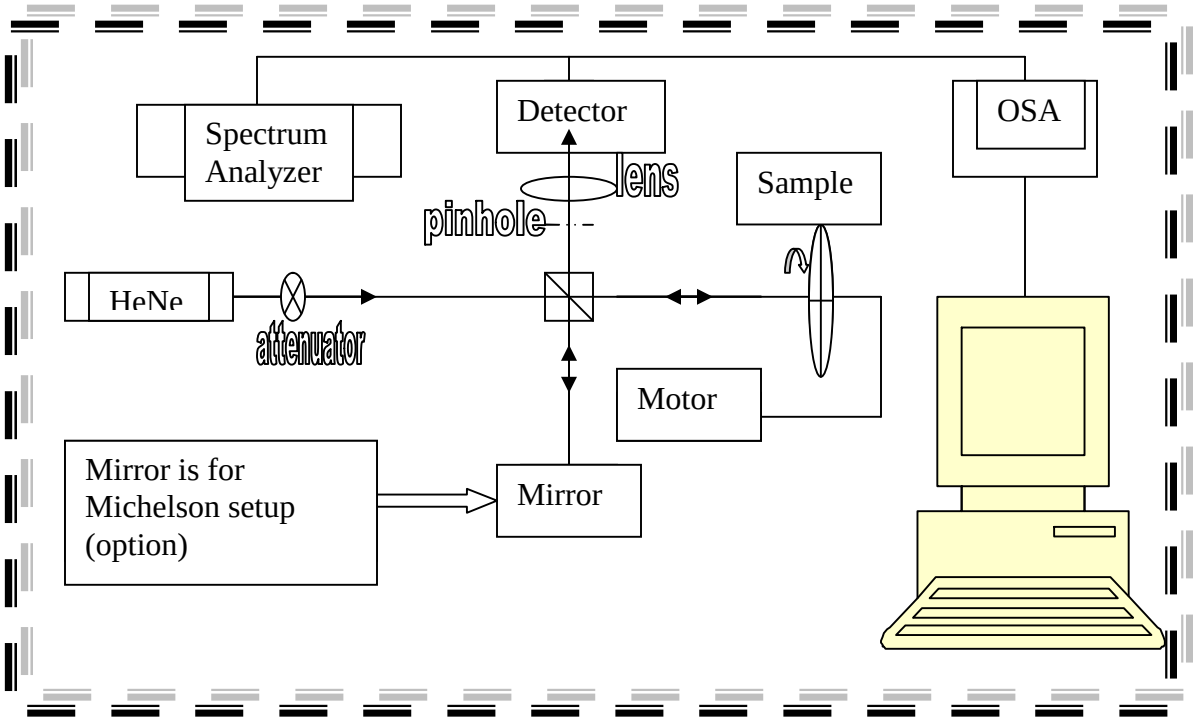

Figure 4.3 Experimental setup for surface roughness measurement.

The 632.8 nm laser light from a He-Ne laser targets onto a wafer with aluminum thin film and steps. When the motor is running, the sample rotates.

The feedback light goes through a pinhole and passes a lens and finally hits a Silicon detector, then caught by a computer. The Fig. 4.4 is the test result.

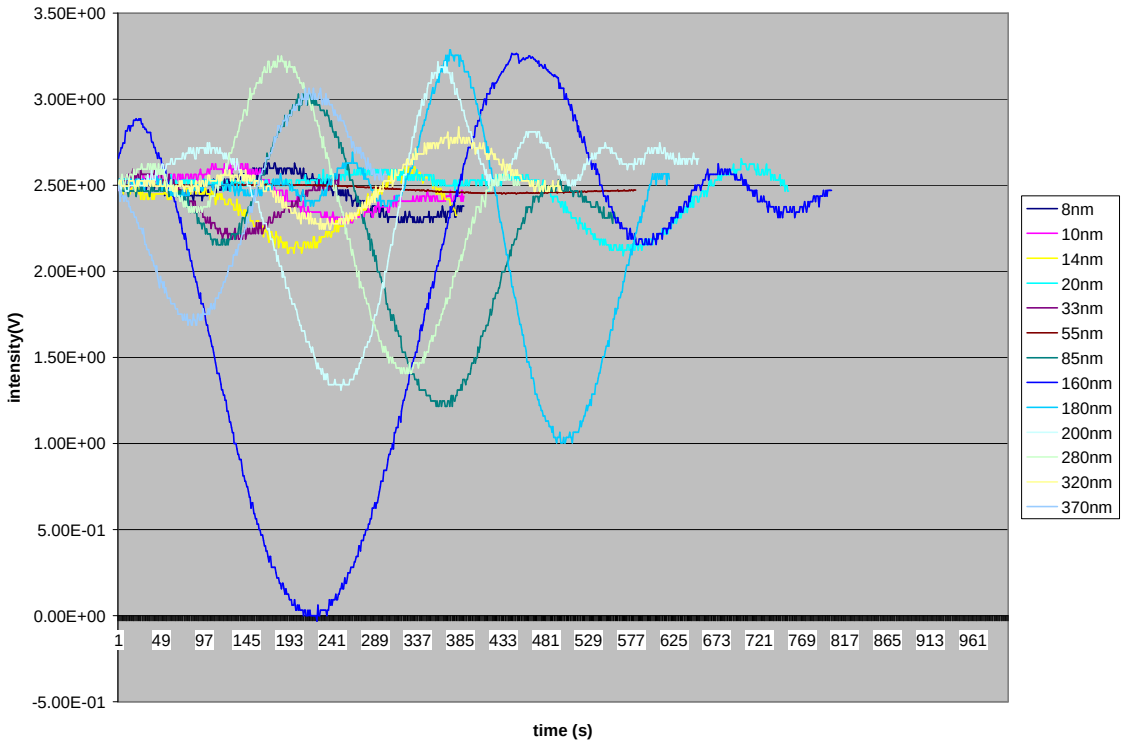

Figure 4.4 Measurement signal of self-interference.

In Fig. 4.4, different step height is corresponding to a curve. When the step height is very small, the amplitude of the signal is very small, which will give small fringe contrast ratio. Once the step height is getting larger, the fringe contrast ratio will be larger. However, if the step height is around 300 nm, the amplitude of the signal will also turn to very small. This phenomenon is because the fringe visibility has a periodical routine of every $l/4$. The Fig. 4.5 shows the fringe contrast ratio from the experiment.

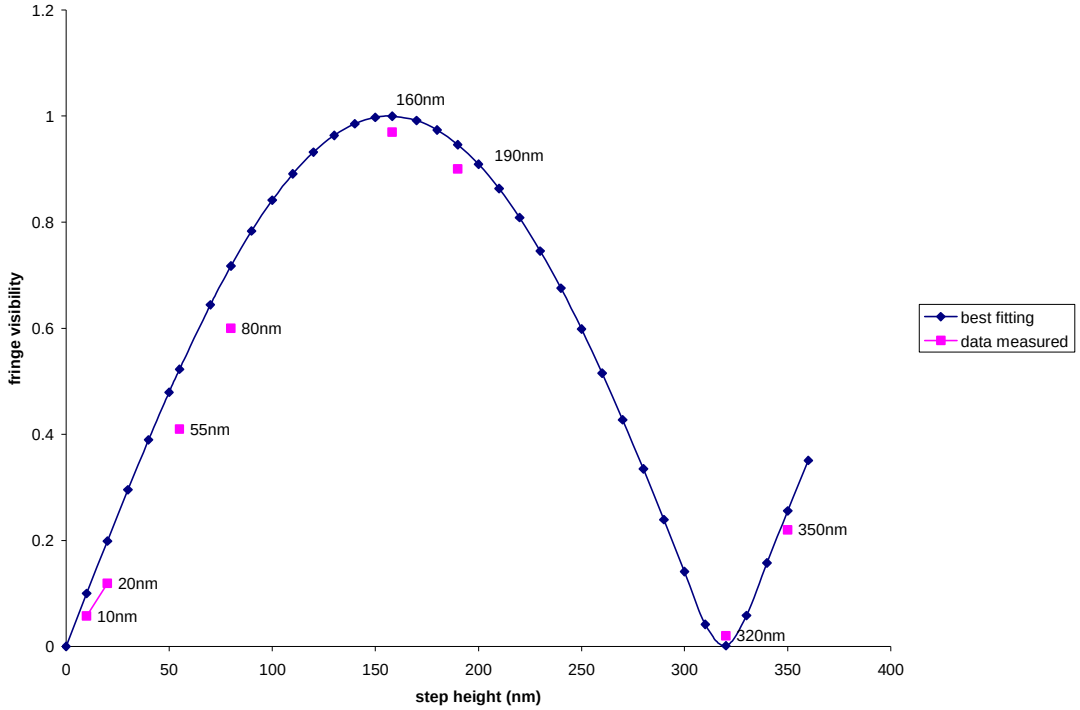

Figure 4.5 Fringe visibility comparison of measurement and calculation.

In Fig. 4.5, the discrete point is related to different steps. The continuous curve is the result from calculation. The measurement data is slightly lower than the theoretical value, which is because the measurement is taken at a small angle (less than 10^{o}). In Fig. 4.4, the pattern shows asymmetry. This is also because the incident angle is not exactly 0 degree. Another important aspect is the size of the detector. The aperture of the detector cannot physically decrease to very small even though the small size detector can provide more accurate contrast ratio of the fringe. On the other hand, if the size of the aperture is too large, it will collect unwanted surface scattering. This result can also show from

the calculation (Fig. 3.6). If the incident angle is not exact zero degree, the highest fringe visibility ratio will happen at larger step height.

For comparison, an optical power meter was employed in the experiment instead of a silicon detector.

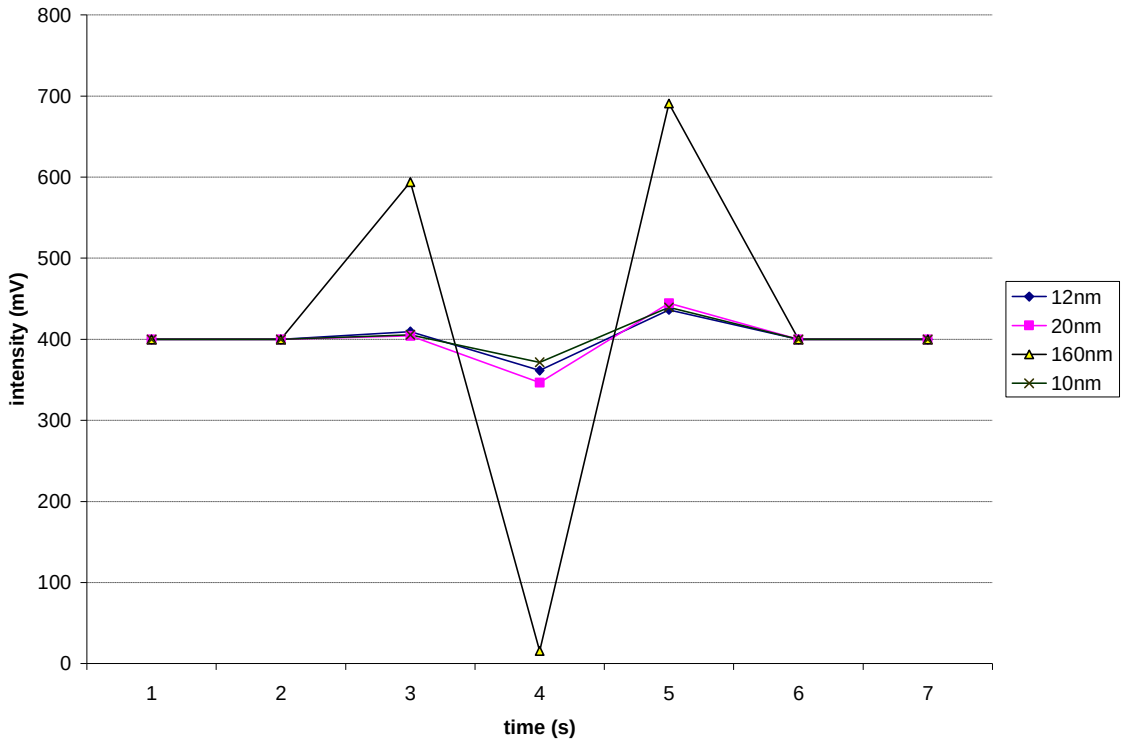

Figure 4.6 Fringe measurements by optical power meter (Model 1830-C from Newport).

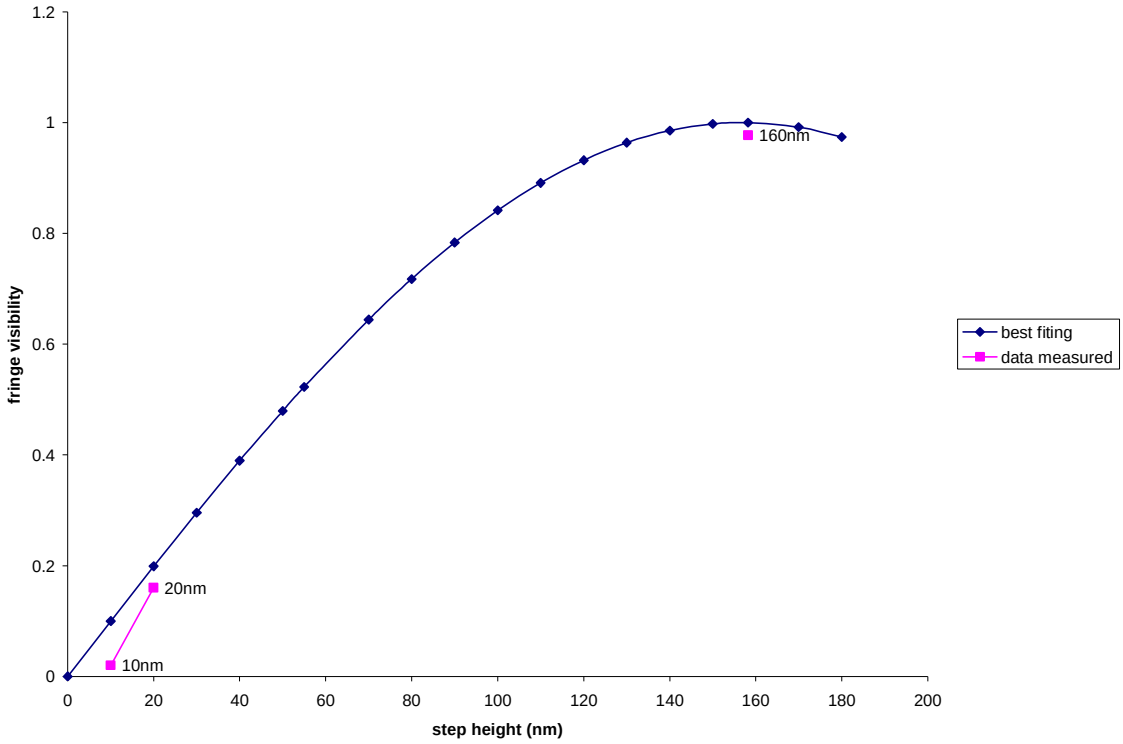

Figure 4.7 Comparison of measurement and calculation (measured by optical power meter (Model 1830-C from Newport).

The above two results are similar, indicating good agreement between the calculation and experiment. As discussed in Chapter 3, the power spectral density from the detected signal should also be considered in the experiment. The next section is regarding power spectral density measurement.

4.2.1.1 Power spectral density measurement (HP 3580A)

To measure the power spectral density of the rough surface when sample is rotating, a silicon detector is used in the experiment. The Fig. 4.8 and 4.9 are from the oscilloscope. The step height of the sample is 200 nm.

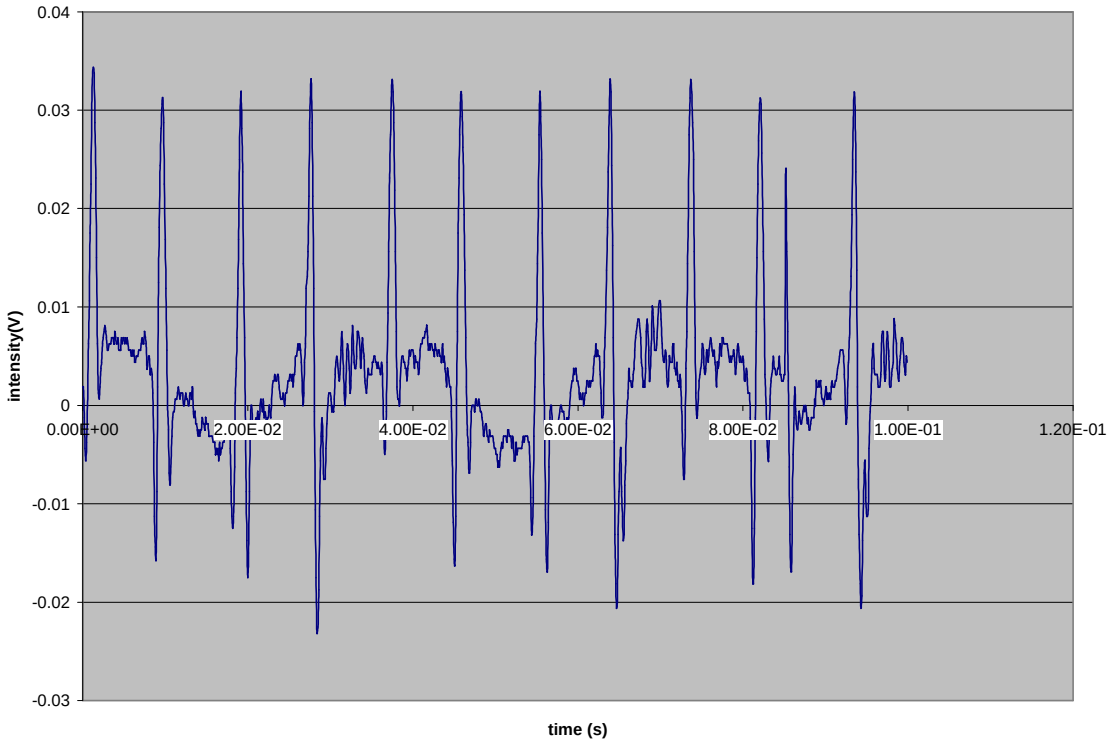

Figure 4.8 Modulated signal when incident beam was out of the border of the step and flat area.

Fig. 4.8 shows the signal from the rotating sample when the incident beam was out of the border of the step and flat area. Fig. 4.9 provides signal from the rotating sample when the incident beam was hitting cross the border of the step area and flat area. Fig. 4.10 shows the location of incident beam.

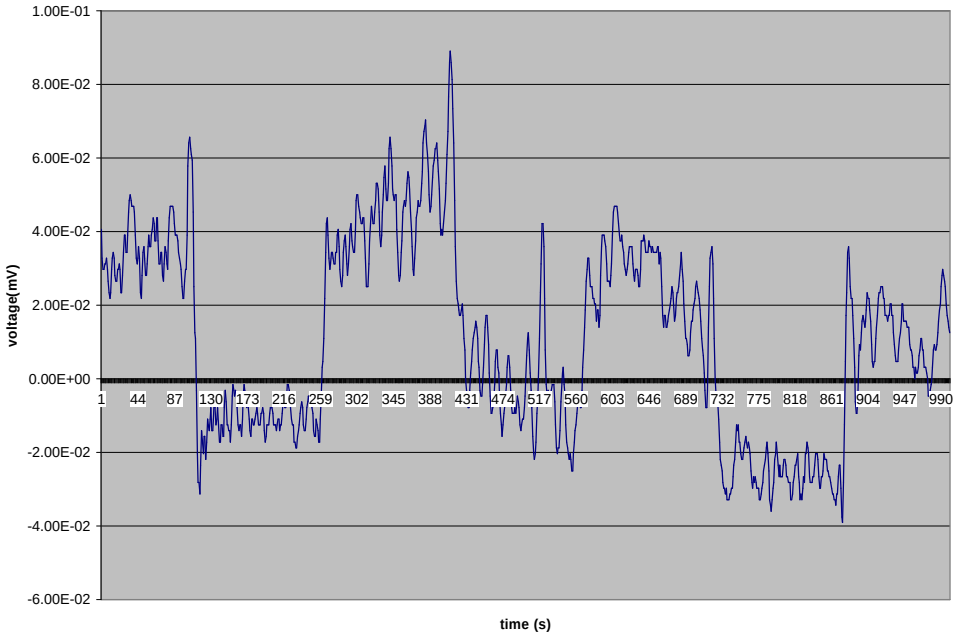

Figure 4.9 Modulated signal when incident beam was covering the border of the step and flat area.

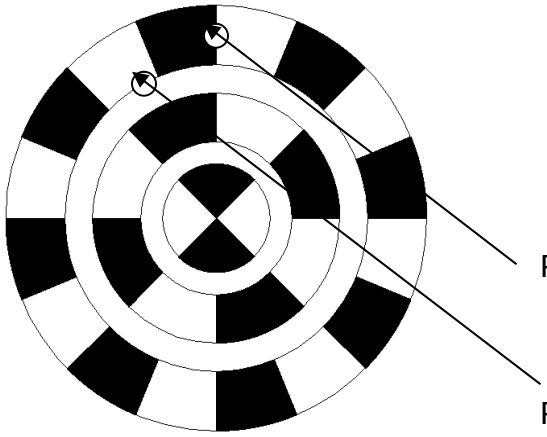

Figure 4.10 Position of the incident beam.

From Fig. 4.8 and Fig. 4.9, the signals have an obvious difference. The signal is pulse train shape when the signal is traveling the step area per turn; the signal is square wave shape when half of the incident beam is on flat area and

the other half is on step area. These two different phenomena are due to the different phase modulation from the rough surface. The following *PSD* measurement is presented when half of the incident beam covers the step area and the other half cover the flat area.

All power spectral density measurements proceeded with the original setting: frequency span=10 *Hz*, sweeping time=200 sec/div, and input sensitivity=0.2 *V* with HP 3580A.

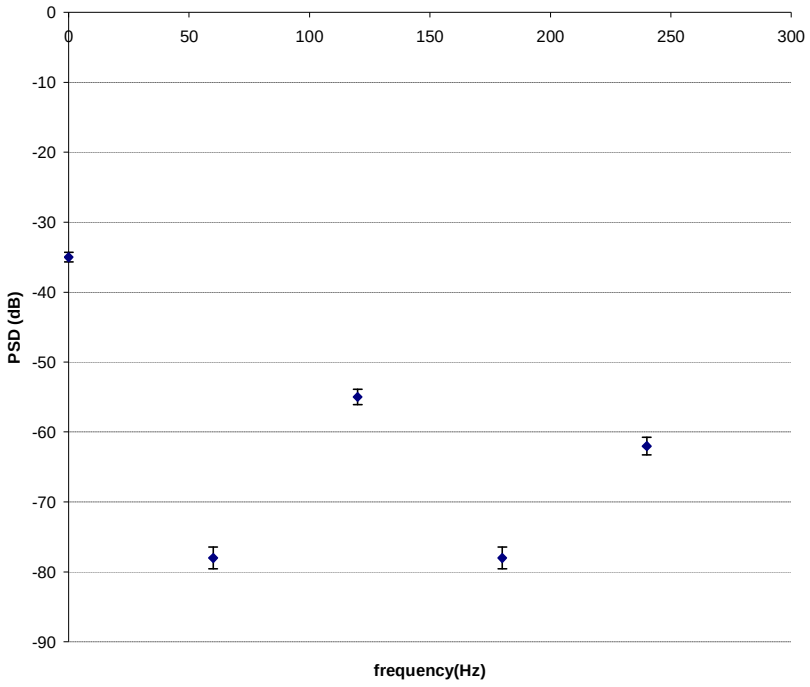

Figure 4.11 *PSD* value of the power lines.

In Fig. 4.11, the *PSD* of the power lines shows that the power lines have strong harmonic at 60 *Hz*, 120 *Hz*, 180 *Hz*, and 240 *Hz*. To achieve relative accurate power spectral value of the measurement, the frequency of the rotation

should avoid 60 *Hz*, 120 *Hz*, 180 *Hz*. Therefore, in this experiment, the rotating frequency is 100 *Hz* which is different from the above frequencies of power lines. Fig. 4.12 provides a comparison of calculation and measurement.

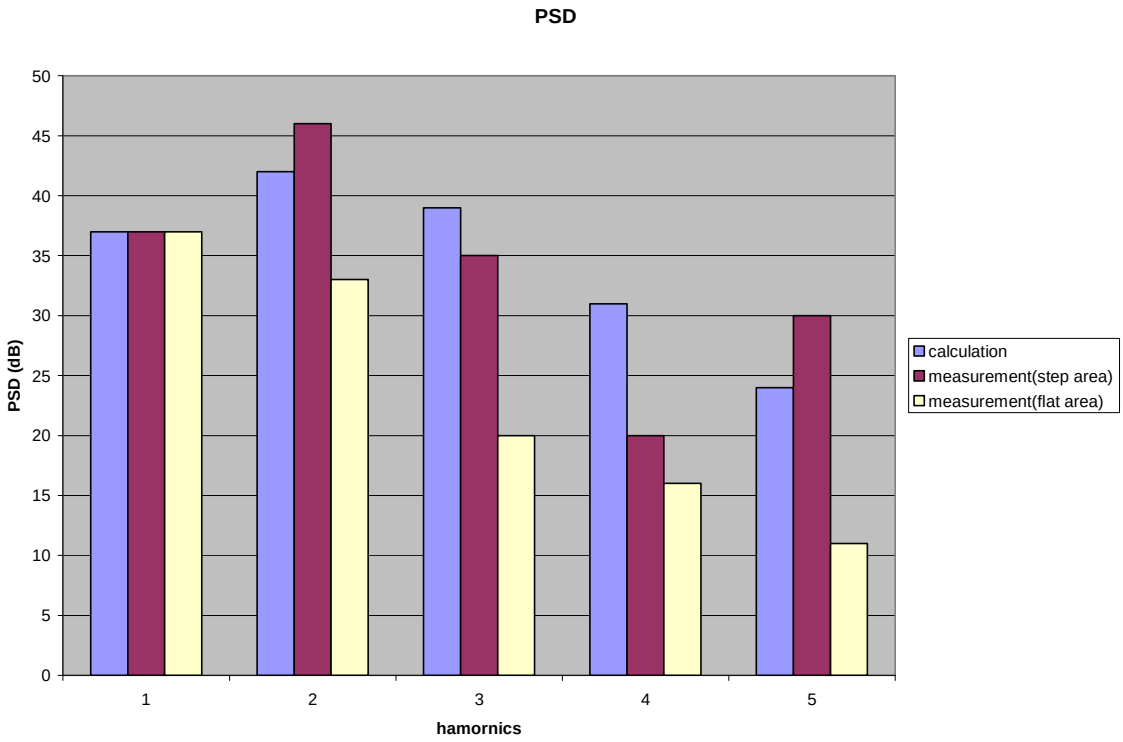

Figure 4.12 Comparison of calculation and measurement results.

In Fig. 4.12, blue data is the result of calculated *PSD*; red data is the result of step area *PSD*; and white data is the result of flat area *PSD* (the flat area is the white ring in Fig. 4.10). One conclusion is that the harmonics' trends are similar for both calculation and measurement. The values are not the same, due to the sensitivity of the signal at the detector.

When the incident beam is only sweeping the step area (Position 1 in Fig. 4.10), the power spectral density measured from HP 3580A is shown below:

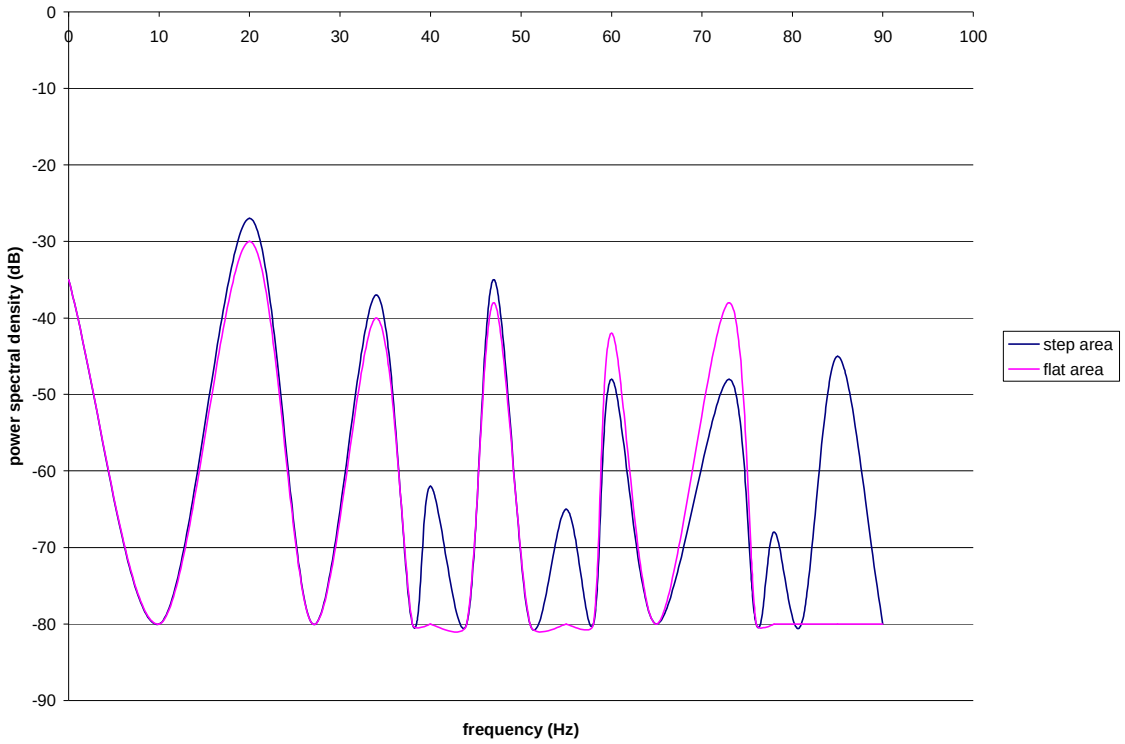

Figure 4.13 Power spectral density measured by HP 3580A.

In Fig. 4.13, the red line is the measurement result of flat area; the blue line is the measurement result of the step area. There is a difference between the two results: the harmonics occur when the measurement is taken from the step area (rough area). For comparison, the power spectral density has also measured by HP 8593E, and the measurement result is shown below:

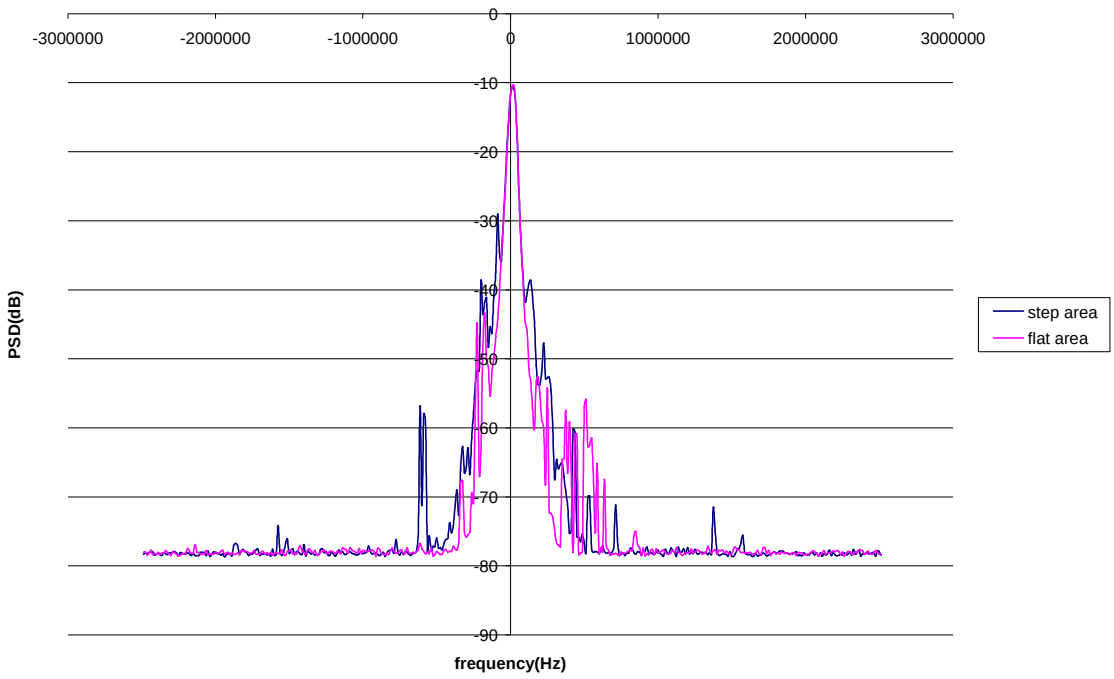

Figure 4.14 Power spectral density measured by HP 8593E.

Same as Fig. 4.13, Fig. 4.14 also shows that the PSD from the step area (rough area) has higher amplitudes of harmonics than the flat area.

4.2.1.2 Summary for *PSD* method

From the *PSD* measurement of the signal detected from a silicon detector, the well-aligned setup can strongly affect the measurement result such as the harmonics' trends. When the sample is rotating, as the mechanical spinning is always waggling, the feedback beam from the sample makes a circle. Currently, there is no efficient way to solve this problem. This is the key problem of the measurement.

4.2.2 Michelson interferometer for surface roughness measurement

Michelson interferometer is also employed in this study in order to compare the difference with self inference method. The following figure is the setup of the measurement for Michelson interferometer [44].

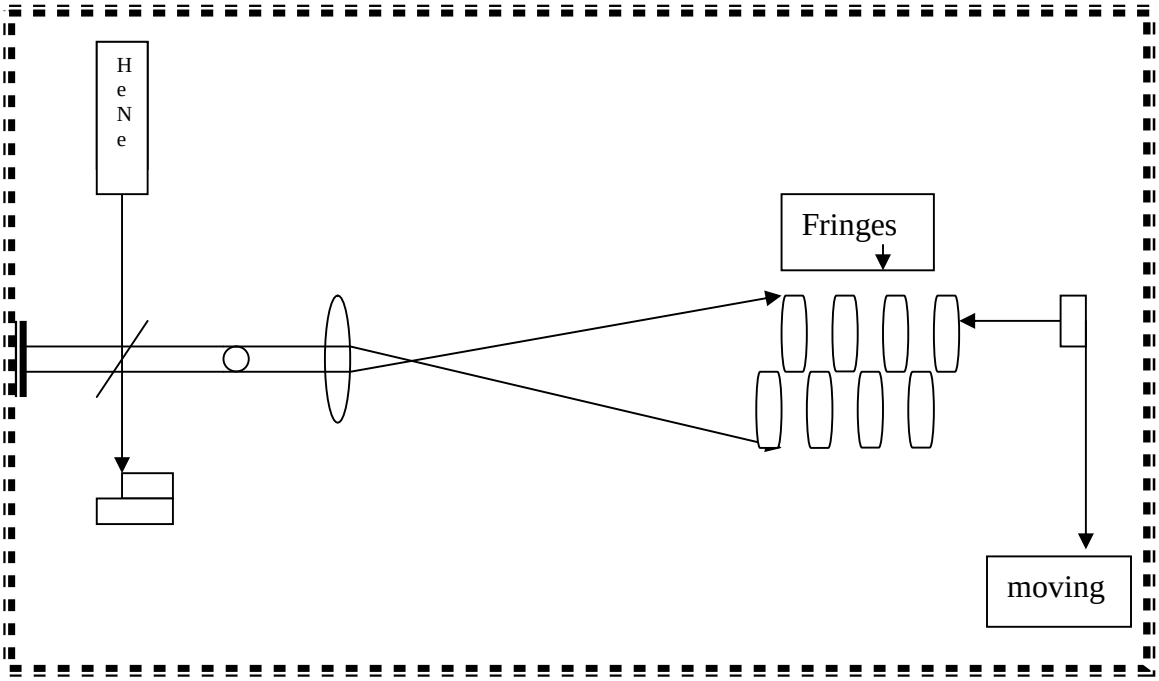

Figure 4.15 Michelson interferometer setup with non-rotating sample.

In above figure, the sample is stationary. The incident beam passes a beam splitter, one half travels to a mirror, whereas the other half travels to a rough sample. The two feedback beams travel back and all pass the beam splitter. The interference fringe on the screen is shown in Fig. 4.15. If a mirror is in place of the sample with step, the fringes are one-group parallel strips. However, due to the step of one sample, the fringes are two group parallel strips, and the shifting space is related to the step height.

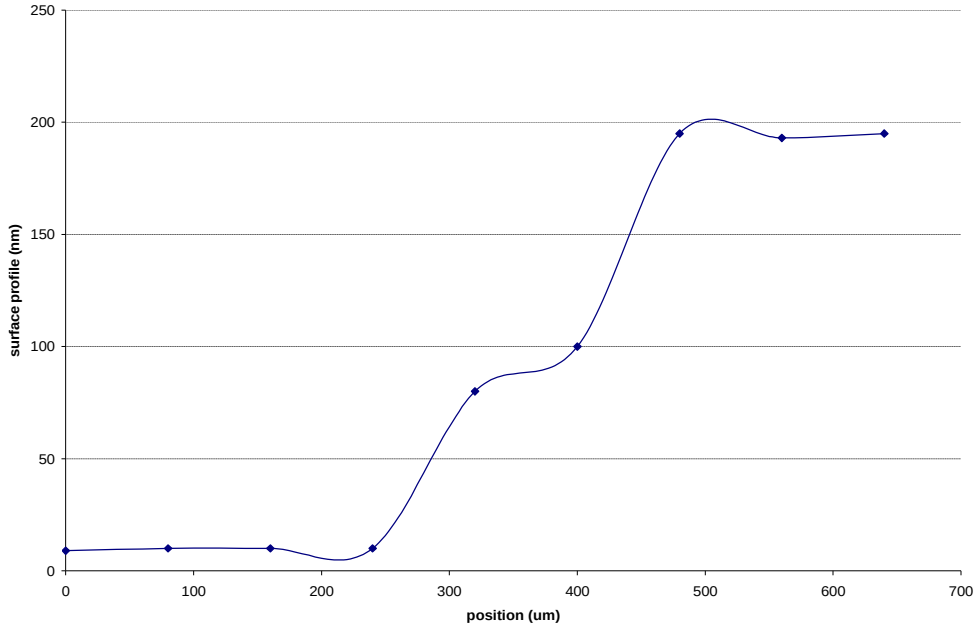

Figure 4.16 Michelson interference measurement without sample rotating.

From the above setup, by enlarging the interference beam size through a lens, and by choosing the value in the middle area to decrease Gaussian shape effect, the amplitude of the fringe corresponding to each point can be achieved. Substituting the voltage value to the calculation formula, the result produces the displacement at each point. The step height value is provided as [44]:

$$h = \frac{a}{d} l \qquad \text{Eq. (4.1)}$$

where h is the step height,

a is the shifting space

d is the distance between two bright strip

l is the incident wavelength

Figure 4.17 gives the relationship of the parameters in Eq. 4.1.

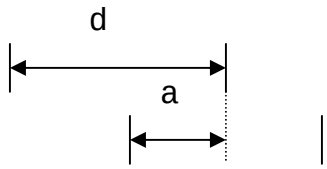

Figure 4.17 Geometry of interference fringes.

Substituting the measurement data to Eq. 4.1, the step height of the result is 180nm, which is very close to the actual value of the step (200 nm). However, if the step height is low (20-100 nm), this kind of method has limitation of accuracy. In this situation, *CCD* camera should be utilized instead of a detector. In above measurement, the sample is stationary. As the goal of this research is to measure a rotating sample, the following measurement was carried out.

In the setup of Fig. 4.3, the sample is rotating. He-Ne laser beam passes the beam splitter. The feed back beams from the rotating sample and mirror travel to the beam splitter. The two beams interfere after a critical alignment. To compare the difference between the flat area and rough area, both situations with rotating sample was measured. Figures 4.18 and 4.19 show the signal measured by a detector.

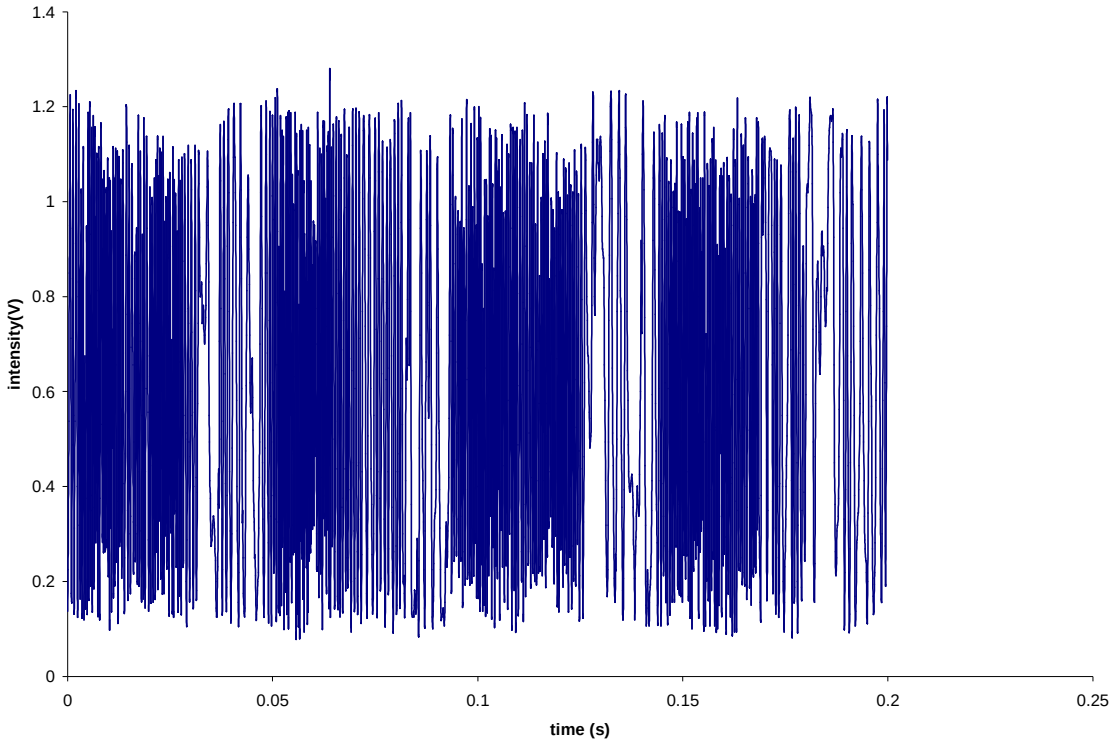

Figure 4.18 Michelson interference measurement at flat area with sample rotating.

From the above data, the vibration of the motor produces the path length change compared to the fixed mirror. The number of the fringes is related to the amplitude of mechanical vibration. This approach can also be used to analyze the vibration problem. The above fringes have 43 fringes, which is corresponding to 21.5 wavelengths path length change. The exact number of the path length difference or the amplitude of the vibration can be calculated by substituting the wavelength into the equation ($2\Delta d=n\lambda$)[47]. For example, the wavelength is 632.8nm, the path length difference is 13605.2 nm, or the amplitude of the vibration is 13605.2nm. In Fig. 4.18, the signals of all the fringes are within a

sinusoidal shape envelope. The reason is due to the vibration of the motor. When the motor is rotating, the feedback or reflection beam makes a small circle, which is due to mechanical problem (ball bearings). This small circle introduces intensity modulation into the signal, which is a low frequency amplitude modulation.

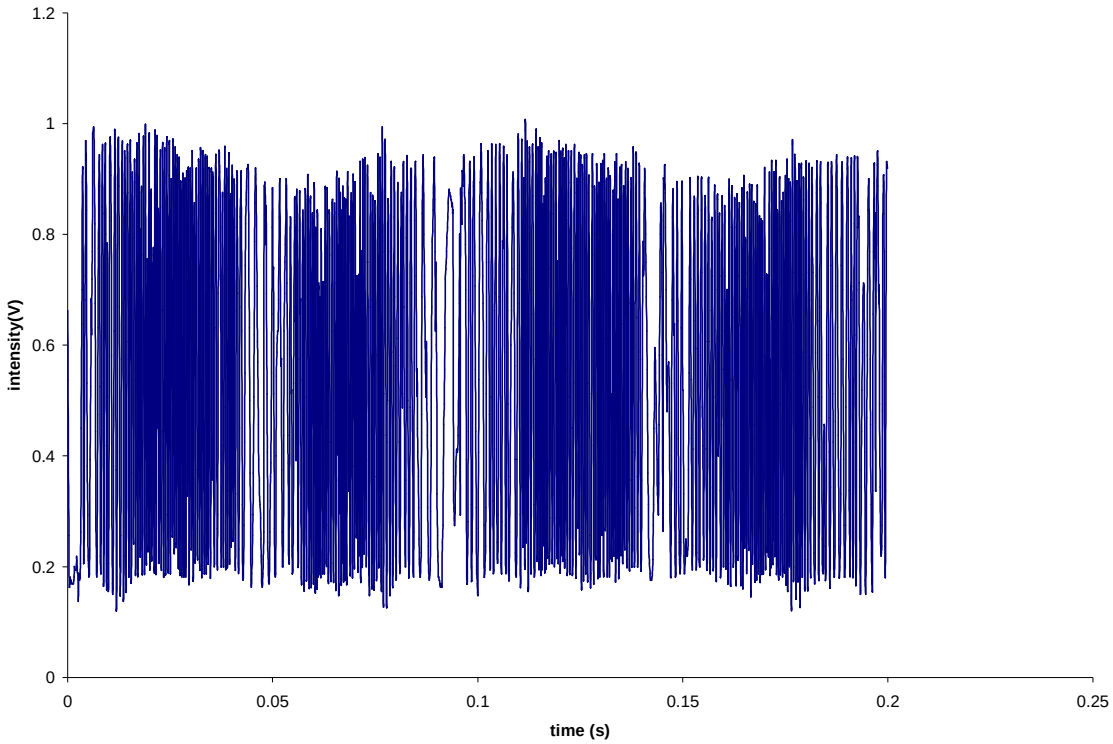

Figure 4.19 Michelson interference measurement at step area with sample rotating.

After Fast Fourier Transform (*FFT*) and power spectral density (*PSD*) applied in the data analysis, the result shows that the lowest harmonic has the highest value at flat area and the lowest harmonic has a little lower value at the

rough area comparing to the flat area. The rougher the surface is, the lower the first harmonic value is.

Fig. 4.19 is scaled and re-plotted in Fig.4 .20:

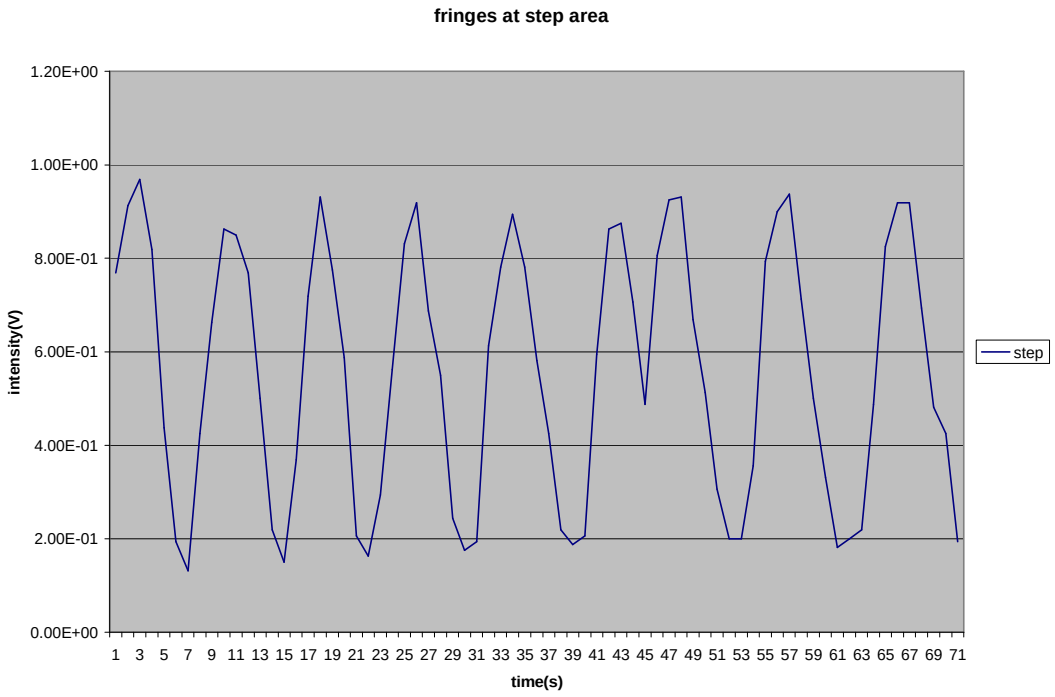

Figure 4.20 Michelson interference data with sample rotating at step area.

In the above figure, there is a sharp or spike between fringe 6 and 7, which is due to the step of the sample (roughness). If there is no step on the sample, the fringes are continuous, as shown in Fig. 4.21:

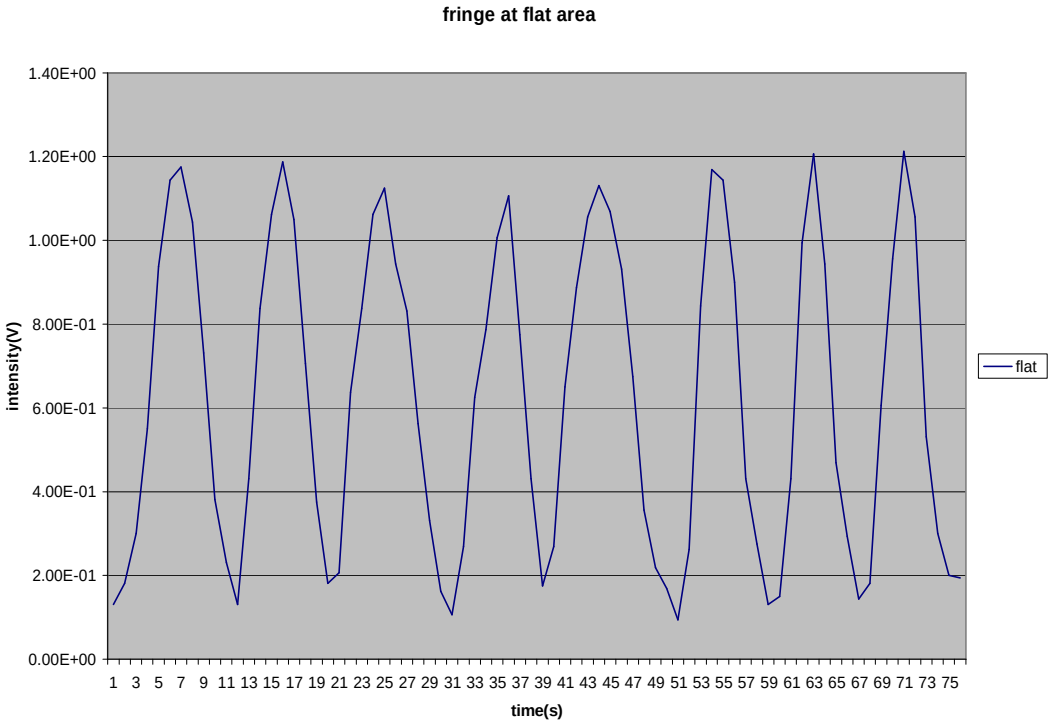

Figure 4.21 Michelson interference data with sample rotating at flat area.

To analyze the shifting or the spike between fringes, a numerical calculation is presented in Fig. 4.22.

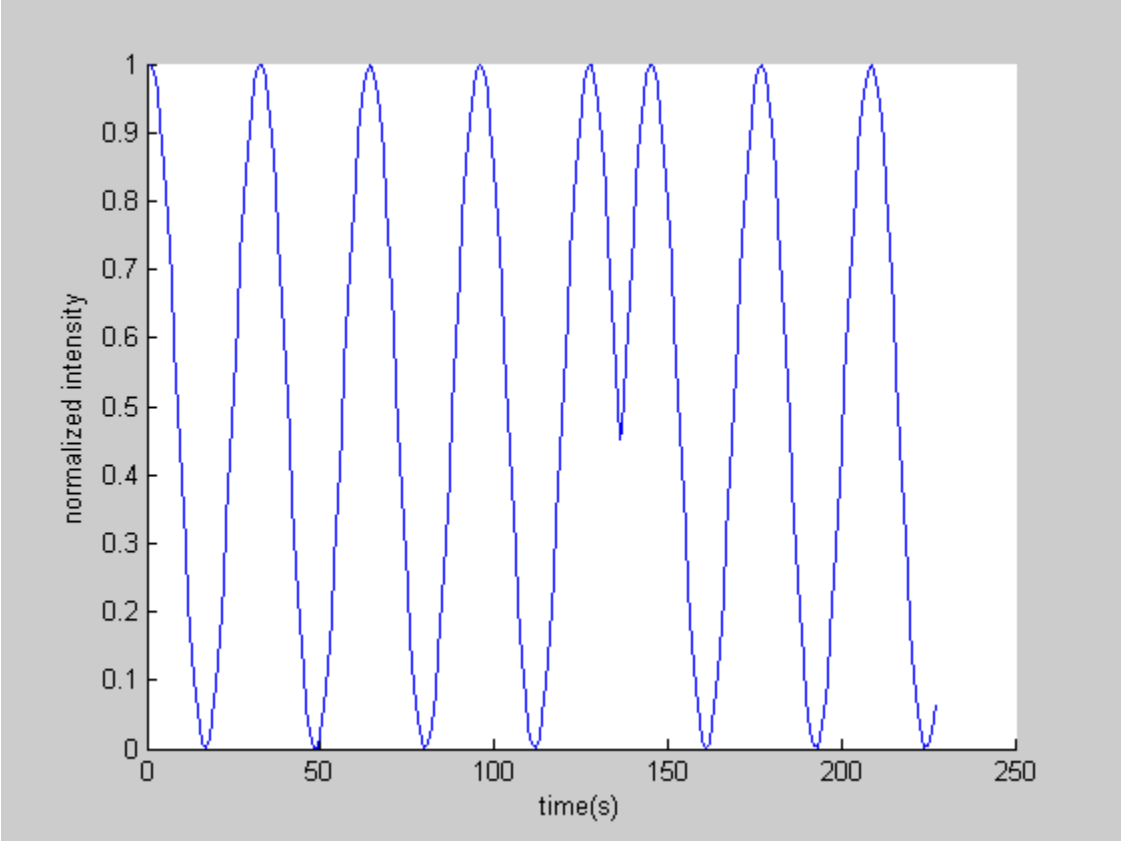

Figure 4.22 Calculation of Path length changing with step (150 nm) in Michelson interferometer (codes in Appendix B and C).

In above figure, the continuous distance changing at one wavelength can produce well-defined cosine or sine wave shape fringes. When the distance change meets one sudden path length jump or step, the cosine or sine wave shape fringes will change their trends. In the time domain there will be a sharp peak. This peak includes the phase jumping or the step height. In the calculation, to get this peak value, the corresponding step height is about 150 nm, which is slightly different with the real value of the step (200 nm). The following figure shows the result of calculation for 210 nm step height sample.

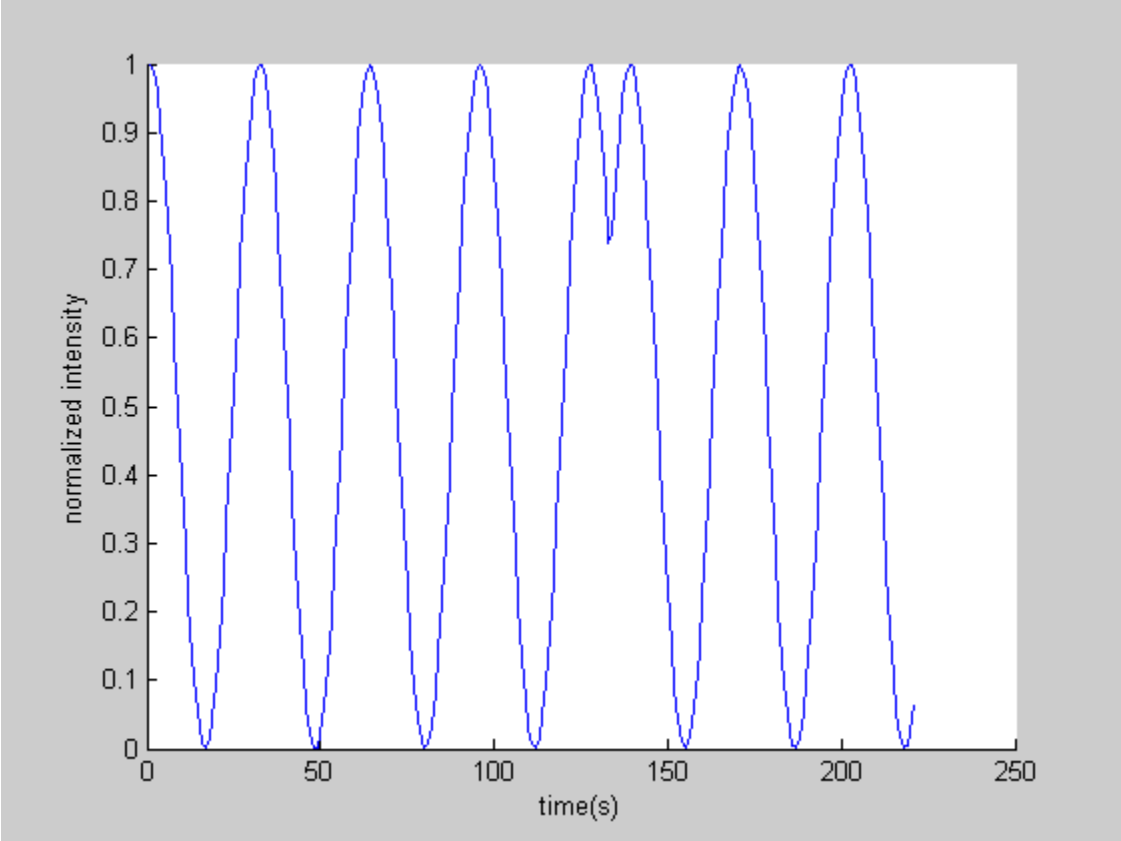

Figure 4.23 Calculation of Path length changing with step (210 nm) in Michelson interferometer.

The difference between the measurement and calculation is due to the amplitudes of the mechanical vibrations involved in the Michelson interference measurement. In other word, the Michelson interference setup with rotating sample is not very successful due to the effect from the mechanical waggling.

For more comparison related to nanometer range roughness measurement, more data from non-optical surface roughness measurement will be provided in the next section.

4.2.3 AFM and Stylus measurement

In this section, the non-optical surface roughness measurements such as atomic force microscope and stylus profiler were carried out.

4.2.3.1 *AFM* measurement

To acquire reference and analyze the data, *AFM* (Atomic Force Microscope) [46] was utilized in this work. For different step sample, each *AFM* picture shows the value of the step height and corresponding shape of the step.

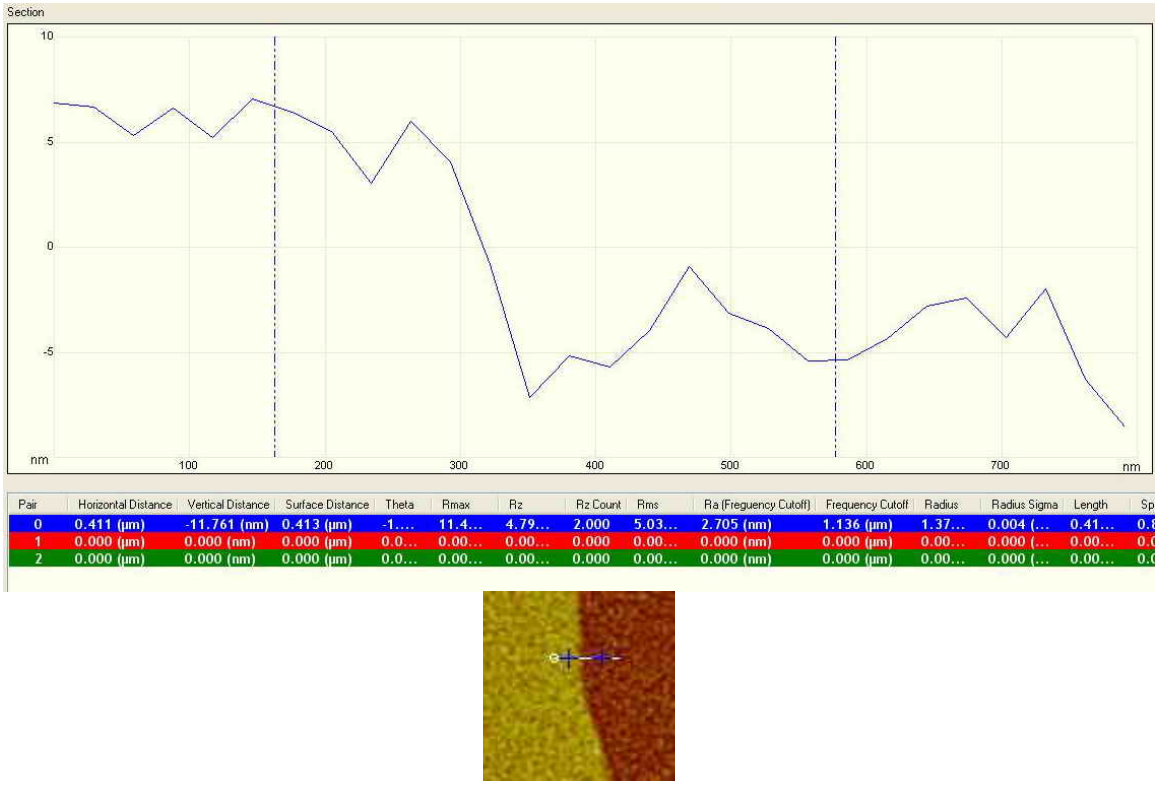

Figure 4.24 12 nm step height sample.

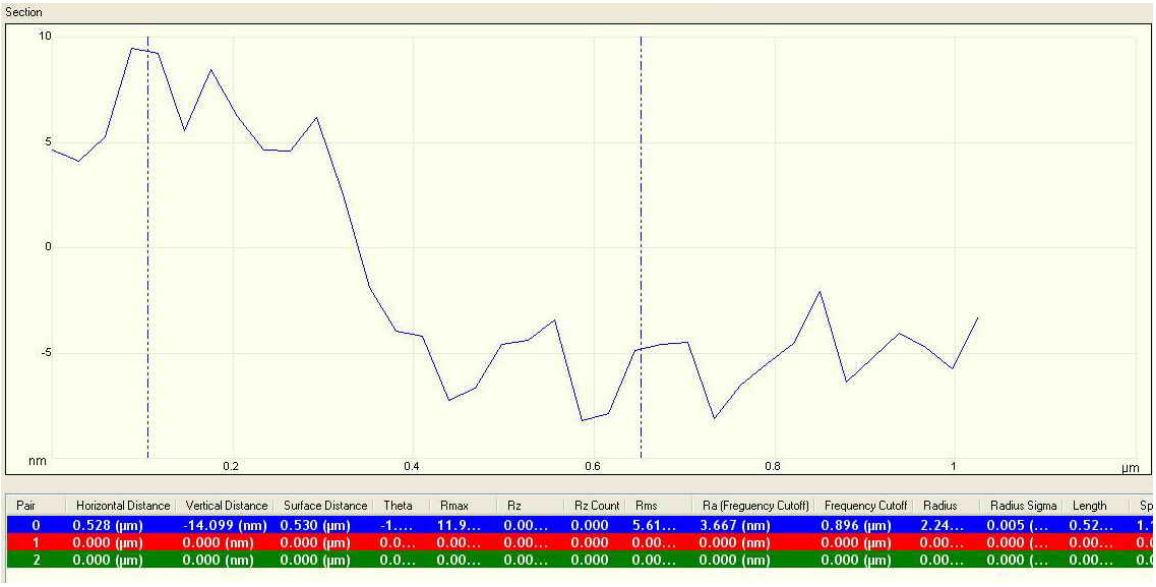

Pair	Horizontal Distance	Vertical Distance	Surface Distance	Theta	Rmax	Rz	Rz Count	Rms	Ra (Freguency Cutoff)	Frequency Cutoff	Radius	Radius Sigma	Length	Sp
0	0.528 (µm)	-14.099 (nm)	0.530 (µm)	-1....	11.9...	0.00...	0.000	5.61...	3.667 (nm)	0.896 (µm)	2.24...	0.005 (...	0.52...	1.
1	0.000 (µm)	0.000 (nm)	0.000 (µm)	0.0...	0.00...	0.00...	0.000	0.00...	0.000 (nm)	0.000 (µm)	0.00...	0.000 (...	0.00...	0.
2	0.000 (µm)	0.000 (nm)	0.000 (µm)	0.0...	0.00...	0.00...	0.000	0.00...	0.000 (nm)	0.000 (µm)	0.00...	0.000 (...	0.00...	0.

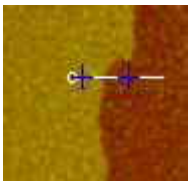

Figure 4.25 14 nm step height sample.

Pair	Horizontal Distance	Vertical Distance	Surface Distance	Theta	Rmax	Rz	Rz Count	Rms	Ra (Freguency Cutoff)	Frequency Cutoff	Radius	Radius Sigma	Length	Sp
0	1.438 (µm)	-19.528 (nm)	1.446 (µm)	-0....	26.0...	9.20...	6.000	7.87...	5.467 (nm)	0.406 (µm)	1.77...	0.045 (...	1.43...	2.4
1	0.000 (µm)	0.000 (nm)	0.000 (µm)	0.0...	0.00...	0.00...	0.000	0.00...	0.000 (nm)	0.000 (µm)	0.00...	0.000 (...	0.00...	0.0
2	0.000 (µm)	0.000 (nm)	0.000 (µm)	0.0...	0.00...	0.00...	0.000	0.00...	0.000 (nm)	0.000 (µm)	0.00...	0.000 (...	0.00...	0.0

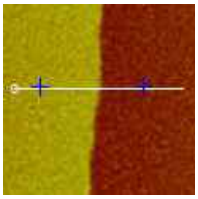

Figure 4.26 20 nm step height sample.

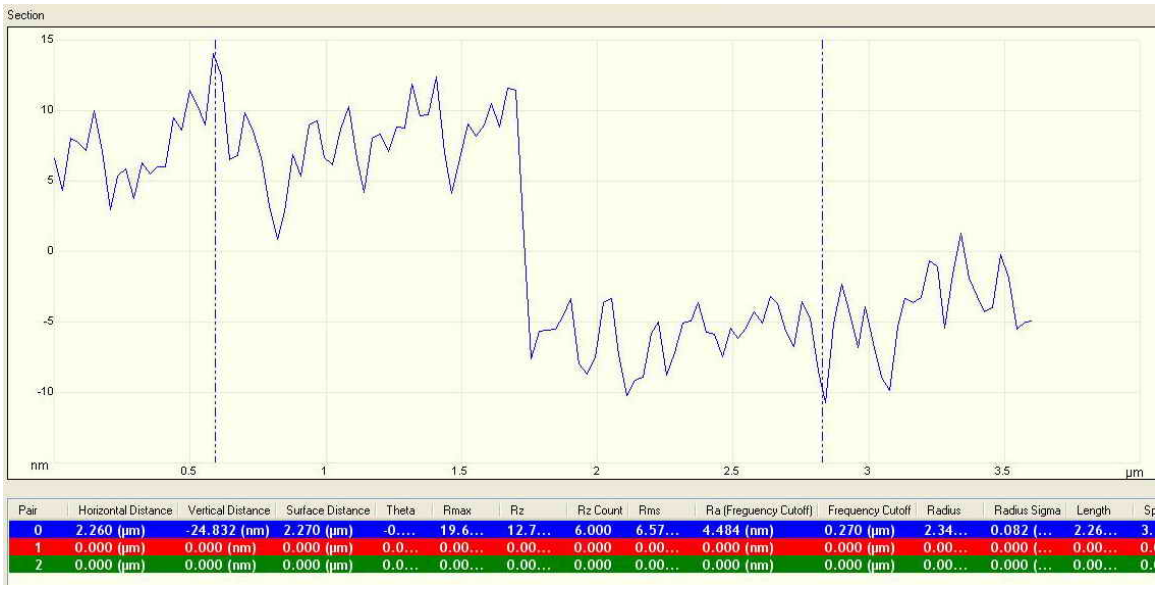

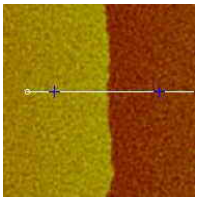

Figure 4.27 25 nm step height sample.

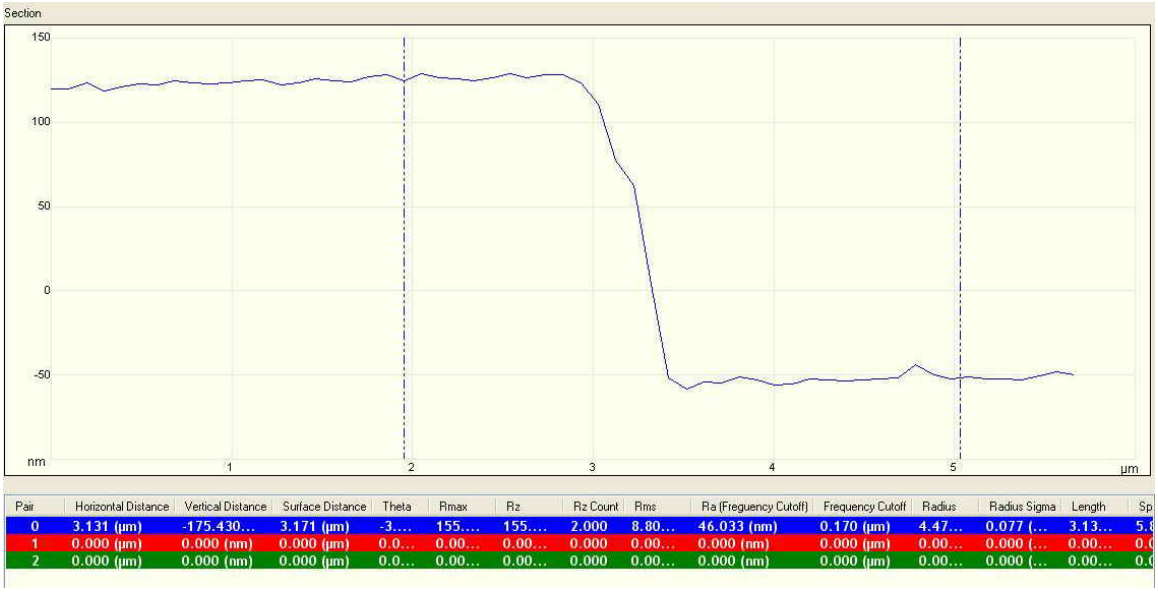

Figure 4.28 175 nm step height sample.

AFM is an accurate method to measure nanometer range thin film sample. However, the measurement range is very short. To acquire larger range data, the alignment time and data analysis time are rather long. The measurement can only be taken when the sample is stationary and located in a clean chamber, which is not applicable for on-site surface roughness measurement.

4.2.3.2 Stylus measurement (Alpha step)

Alpha step is mainly used in clean room environment. For larger step height, Alpha step has advantages such as convenience and accuracy, etc. However, when step height is small enough compared to nanometer range,

alpha step instrument has some disadvantages such as over sensitive to vibration, oversize to the stylus' tip.

To compare Alpha step and *AFM*, the follow figure shows the difference.

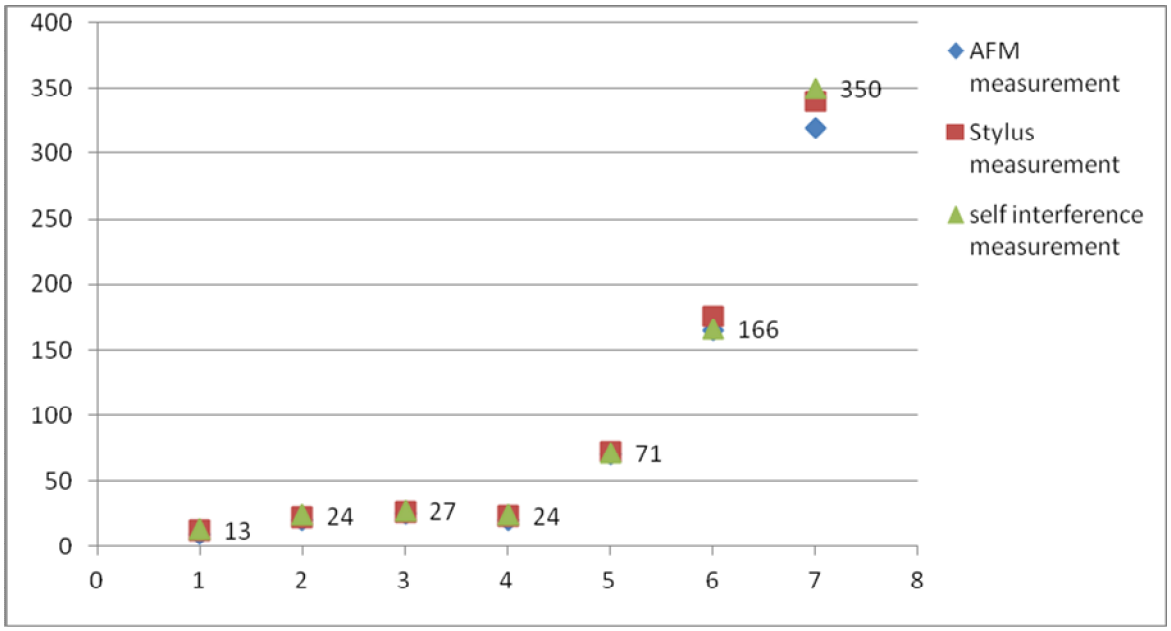

Figure 4.29 Results of *AFM*, Stylus and self interference measurements.

From the above figure, the 320nm step sample is measured by Alpha step as 350 nm. The overall deviation is within ± 10 nm. The detail comparison for different measurement instruments will be discussed in the next chapter.

4.3 Summary

The samples with different step heights were measured in self-interference setup, Michelson interferometer, and *AFM* and mechanical stylus. All measurement techniques demonstrate the advantages. *AFM* and stylus are commercially available and employed in industry, but these two methods are not suitable for on-site surface roughness measurement. Michelson interferometer also has the same problem for a rotating sample, as mechanical influence is involved and inevitable. Only self-interference method is relatively applicable, because self-interference method is not affected by mechanical rotating and does not need long time alignment.

Chapter 5

Conclusion and Future Work

5.1 Conclusion

This research was attempted to integrate the optical theories of interference and scattering for a non-contact on-site surface roughness measurement on the nanometer level. The objective has been reasonably archived:

a). Methodology

This research is to explore and verify a new method to measure surface roughness. The theory in this new method is self-interference.

b). On-site measurement

There is no literature reported for on-site surface roughness measurement with rotating sample. Novelty of this work is that the rotating sample was measured in self-interference setup.

c). Roughness range

Samples with different step heights from 12 nm to 300 nm were measured. The entire measurement results can be obtained for the full cycle. When the step height exceeds $l/4$, the interference fringe will reproduce periodically.

To get higher resolution of roughness measurement, self-interference is a good solution, because self-interference fringe is not disturbed by environment and noise.

The following sections provide discussions on some problems in the measurement and some suggestion for future works.

5.2 Problems

5.2.1 Problems from self-interference

From the trends of the power spectral density, it can be concluded the first harmonic is the strongest peak when the sample has lower step height or relatively smooth (<< $l/4$). Therefore, the first order harmonic is an important parameter for this step measurement. For example, if an unknown height (230 nm) of a sample was measured, by substituting the amplitude of the first order spectrum into the calculation, the height of the step can be calculated. However, if the trends show higher order harmonics with higher amplitudes, which means the height exceeds 230 nm. There should be a jump of the step. Also, if the height of the sample is below $l/4$, the first order has the strongest peak.

The disadvantages of *PSD* measurement and calculation of power spectral densities include:

a). Currently, there is still no commonly accepted criterion whether one-sided or two-sided *PSD* should be calculated, although two-sided calculation is preferred.

b). Subjectivity in parameter settings of electronic spectrum analyzers, especially the detector mode and averaging method.

c). Ineffective failure mode setting of correction factors (e.g. for the effective noise bandwidth) to data obtained with electronic spectrum analyzers.

d). Mechanical vibration in the current setup, which significantly influence the *PSD*.

f). The alignment in the setup also randomly introduces errors to the *PSD*.

5.2.2 Problems from Michelson interferometer

From the current setup and samples, mechanical vibration is involved in the interference fringes. If the vibration is a non-sinusoidal function, more complicated data analysis should be taken into account. Beside mechanical vibration, if the sample surface has big waviness, the interference pattern or the fringe will distort, which requires even more complex shape analysis (deformation out of plane). The environment problems, such as airflow and air pressure, temperature, interrupt the interference in Michelson interferometer all the time.

5.3 Future work

In this section, some suggestions and explanations for the future work will be presented.

5.3.1 Multi-wavelength measurement

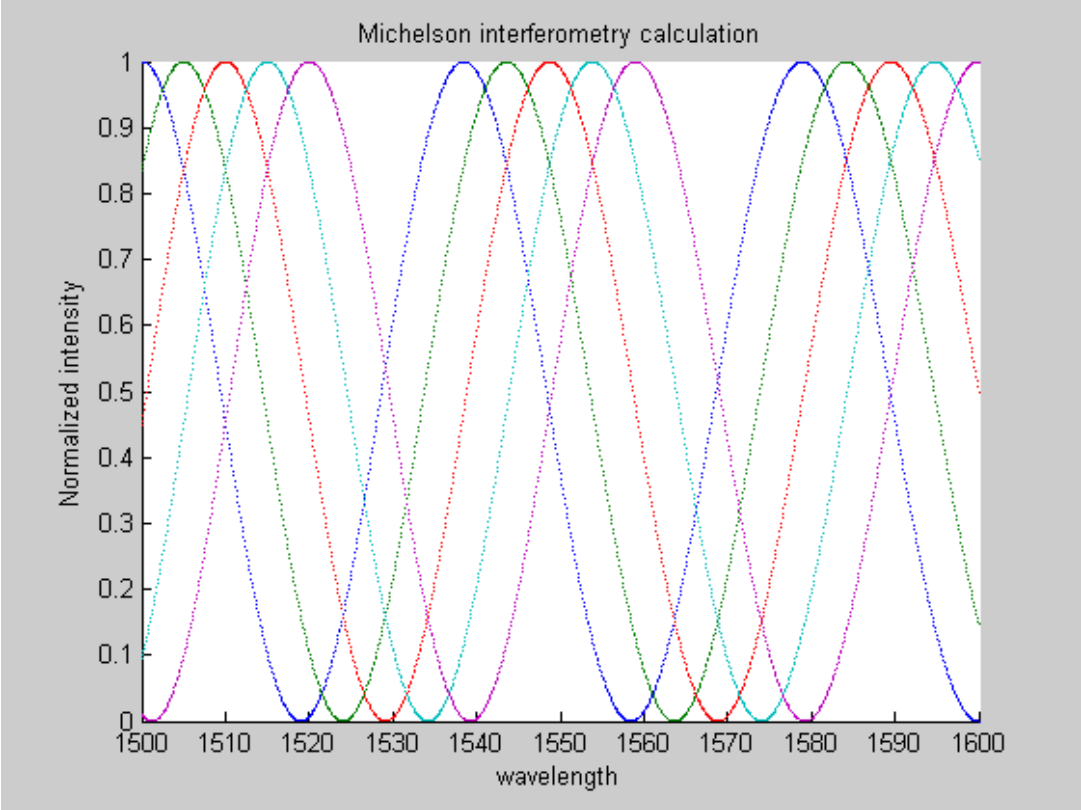

Figure 5.1 Calculation of interference with relative path length change (100 nm).

In Fig. 5.1, when the absolute path length difference is 30000 nm (first blue one), the relative distance change is 100 nm (green, red, green-blue, purple).

By using multi wavelengths and curve fitting, a clear fringe shifting can be measured with current noise level.

However, if relative path length difference is within 30 nm, the calculation of the fringe is shown in Fig. 5.2.

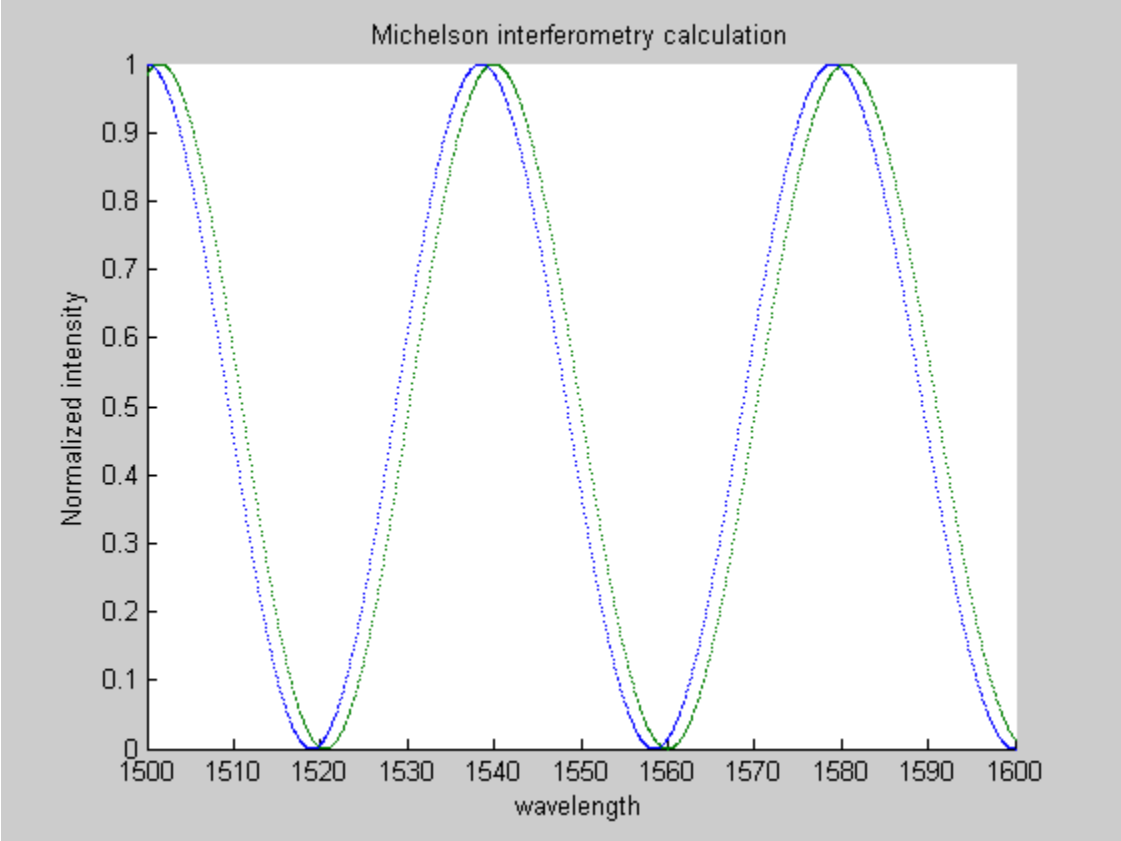

Figure 5.2 Calculation of interference with relative path length change (30 nm).

In Fig. 5.2, when the relative distance change is less than 30nm, the multi-wavelength method at long wavelength also does not have advantage.

To obtain an absolute distance or step height by using Michelson interferometer, Fig. 5.3 indicates the difference between lower wavelength and longer wavelength.

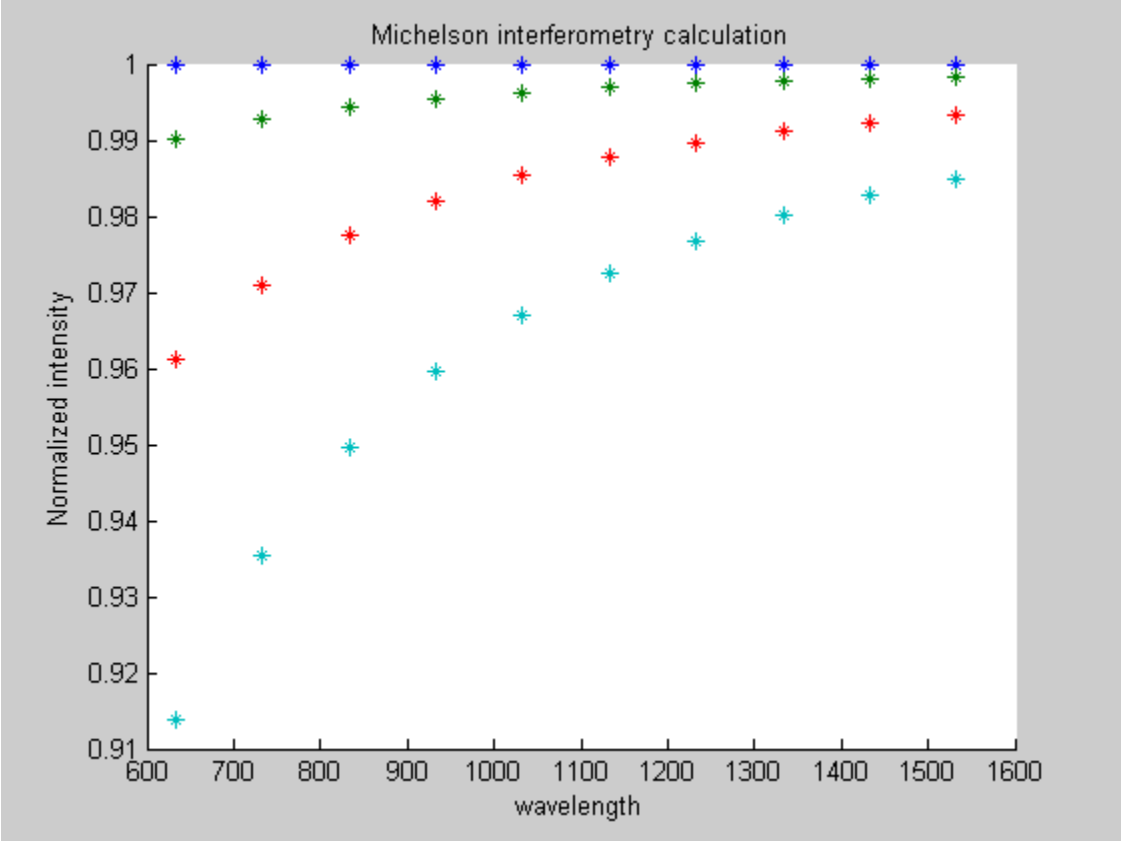

Figure 5.3 Calculation of interference with absolute path length change with wavelength change.

The blue line is 0 nm step, green one is 10 nm, red one is 20nm and green-blue one is 30 nm. In this figure, one problem for small steps is that the fringe visibility decreases to 0. Even though the multi-wavelengths at infrared range are introduced, the fringe visibility is already close to 0 for 30 nm steps.

The challenge for the measurement instrument is to demonstrate a difference in the accuracy to thousandth of unit one. This means the range of phase difference is not suitable for longer wavelength laser source. The multi-wavelength at infrared range cannot help the measurement, either.

For a longer wavelength laser source, the larger roughness sample could be measured more accurately (figure 5.4), because the fringe visibility is still located in the linear region at longer wavelength for larger roughness sample (100 nm < *RMS* < 300 nm). Also, the resolution and accuracy will be improved if multi-wavelength measurement is chosen.

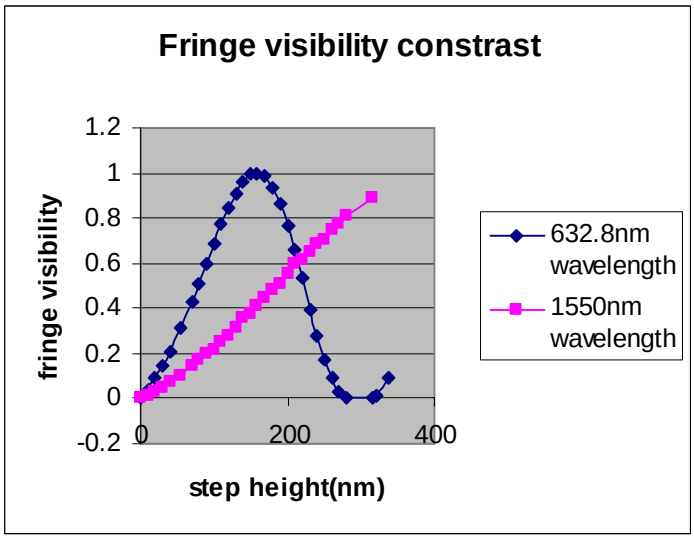

Figure 5.4 Calculation of self-interference at different wavelength.

Therefore, the calculation shows that multi-wavelength method has advantage for roughness at 100 nm < *RMS* < 400 nm. The current roughness measurement technique only involves the roughness less than quarter

wavelength ($l/4$). If multiple fringes at vertical direction (roughness) exist, multi-wavelength measurement is more applicable.

5.3.2 Design and process different samples

In this work, only one structure of rough surface is investigated and analyzed. For future work, higher density steps with different shape such as sinusoidal or triangle or regularly machined sample should be investigated.

5.3.3 *CCD* image for signal analysis

If samples have very high spatial frequency, a *CCD* camera of high precision should be employed for data acquisition. Modern technique provides very high resolution for surface imaging, which can perform more accurate and fast sampling.

5.3.4 Mechanical mounting and physical operation

Current setup has some disadvantages in sample mounting and cleaning. The future work should improve the mounting method and keep clean area for sample measurement, because the defection of the sample surface can produce noise or unwanted signals.

5.3.5 Simulation work

More simulation work should be carried out with complicated step shapes that are closer to real sample roughness.

5.3.6 Other approaches

The inside of the sample (wafer) may have back reflection (especially the mirror). Some lights can be absorbed by material of the sample. In these situations, new non-optical measurement methods [48] should be considered.

References

[1] Gao, Z., Zhao, X.Z., *Diffraction Equations For Weak Scattering Reflective Surface*, Optics and Laser Technology, Vol. 41, No. 3, pp. 303-309, April, 2009.

[2] Lu, R.S., Tian, G.Y., Gledhill, D., Ward, S., *Grinding Surface Roughness Measurement Based On The Co-Occurrence Matrix Of Speckle Pattern Texture,* Applied Optics, Vol. 45, No. 35, pp. 8839-8847, December, 2006.

[3] Whitefield, R.J., *Noncontact Optical Profilometer*, Applied Optics, Vol. 14, No. 10, pp. 2480-5, October, 1975.

[4] Leonard, L.C., Toal, V., *Roughness Measurement Of Metallic Surfaces Based On The Laser Speckle Contrast Method*, Optics and Lasers in Engineering, Vol. 30, No. 5, pp. 433-440, November, 1998.

[5] Sommargren, G. E., *Optical Heterodyne Profilometry*, Applied optics, Vol. 20, Issue 4, pp. 610-618, 1981.

[6] Wang, K.F., Tieu, A. K., *Theory And Experiment Of Spatially And Temporally Partially Coherent Speckle Shearing Interferometry*, Optics and Laser Technology, Vol. 36, No. 1, pp. 43-55, February, 2004.

[7] Ooki, H., Iwasaki, Y., Iwasaki, J., *Differential Interference Contrast Microscope With Differential Detection For Optimizing Image Contrast*, Applied optics, Vol. 35, Issue 13, pp. 2230-2234, 1996.

[8] Jo, M.S., Oh, M.S., *Data Averaging Effect On Roughness Measurement Using Phase-Shifting Interferometry For A Few-Ten-Angstrom And Sub-*

Angstrom Rough Surfaces, Japanese Journal of Applied Physics, Review Papers, Vol. 40, No. 7, pp. 4736-4740, July, 2001.

[9] Bradley, C., *Automated Surface Roughness Measurement*, Advanced Manufacturing Technology, Springer-Verlag London limited, pp. 668-674, 2000.

[10] Valliant, J. G., Foley, M.P., Bennett, J.M., *Instrument For On-Line Monitoring Of Surface Roughness Of Machined Surfaces*, Opt. Eng., Vol. 39, pp. 3247, 2000.

[11] Creath, K. and Wyant, J. C., *Absolute Measurement Of Surface Roughness*, Applied Optics, Vol. 29, No. 26, pp. 3823-3827, 1990.

[12] Jchida, S., Sato, H., O-hori, M., *Two Dimensional Measurement Of Surface Roughness By The Light Sectioning Method*, CIRP Annals, Vol. 28, No. 1, pp. 419-423, 1979.

[13] Church, E. L., Jenkinson, H.A., Zavada, J.M., *Measurement Of The Finish Of Diamond-Turned Metal Surfaces By Differential Light Scattering*, Optical Engineering, Vol. 16, No. 4, pp. 360-374, Jul-Aug, 1977.

[14] Beckmann, P., Spizzichino, A., *The Scattering Of Electromagnetic Waves From Rough Surfaces*, Goford, New York, Pergamon Press, 1963.

[15] Sawatari, T., Zipin, R.B., *Optical Profile Transducer*, Proceedings of the Society of Photo-Optical Instrumentation Engineers, Vol. 153, pp. 8-13, 1978.

[16] Maradudin, A. A., *Light Scattering and Nanoscale Surface Roughness*, Springer, 2007.

[17] Enshasy, H.M., Cassidy, D.T., *Sub-Micrometer Distance Measurements With A Broadly Tunable Short-External-Cavity Ingaasp/Inp Diode Laser,* IET Optoelectronics, Vol. 1, No. 4, pp. 157-162, 2007.

[18] Gupta, P.C., Singh, K., *Holographic Interferometry Of Non-Sinusoidal Vibrations,* Opto-Electronics, Vol. 6, No. 4, pp. 305-311, July, 1974.

[19] Rumelhart, R.D., Mc.Clelland, J., *Parallel Distributed Processing*, Ist Ed., MIT Cambridge Press, 1986.

[20] Al-Refai, A. S. *Surface Roughness Measurement Using Laser Detection Technique,* Master's thesis, 1997.

[21] http://www.grahamoptical.com/phase.html

[22] Thomas, T.R., *Surface Roughness Measurement: Alternatives To The Stylus*, Metrology and Inspection, Vol. 11, No. 2, pp. 9-13, March, 1979.

[23] Youl, J.W., Kim, D., Ryul, S. Y., Kim, S., *Simultaneous Measurement Method Of Total And Self-Interference For The Volumetric Thickness Profilometer,* Optics Express, Vol. 17, No. 3, 1352, February, 2009.

[24] Degarmo, E. P., Black, J T., Kohser, R.A., *Materials And Processes In Manufacturing* (9th ed.), Wiley, pp. 223, 2003.

[25] Yang, L.X., Colbourne, P., *Digital Laser Microinterferometer And Its Applications*, Optical Engineering, Vol. 42, No. 5, pp. 1417-1426, May 2003.

[26] US patent [6016684]

[27] He, G., Jiang, H., Tan, X.W., *Sinusoidal Phase Modulating Interferometer For Real-Time Surface Profile Measurement*, Optica Applicata, Vol. 38, No. 2, pp. 413-420, 2008.

[28] Leit, M.N., Moura, M.F., *Acquisition In Phase Demodulation: Application To Ranging In Radar/Solar Systems* IEEE Transactions on aerospace and Electronic Systems Vol. 31, No. 2, pp. 581-599, April, 1995.

[29] Ohlidal, M., Prazak, D., *Digital Laser Speckle Spectral Correlation Within The Framework Of The Fresnel Approximation Of The Scalar Kirchhoff Theory And Its Application In Surface Roughness Measurement*, Journal of Modern Optics, Vol. 50, No. 14, pp. 2133-2146, 2003.

[30] Zheng, Z.R., Zhou, J., Gu, P.F., *Roughness Characterization Of Well-Polished Surfaces By Measurements Of Light Scattering Distribution,* Optica Applicata, Vol. XL, No. 4, pp. 811-818, 2010.

[31] Snyder, W.C., *Reciprocity Of The Bidirectional Reflectance Distribution Function (BRDF) In Measurements And Models Of Structured Surfaces*, IEEE Transactions on Geosicence and remote sensing, Vol. 36, No. 2, pp. 685-691, March, 1998.

[32] Stover, J.C., *Requirements And Suggestions For Industrial Smooth Surface Microroughness Standards*, SPIE, Vol. 2862, Proceedings, 8-9 August, Denver, Colo., pp. 69-77, 1996.

[33] Church, E. L., Zavada, J. M.**,** *Residual Surface Roughness Of Diamond-Turned Optics*, Applied Optics, Vol. 14, No. 8, pp. 1788-1795, 1975.

[34] Erf, R. K., Chapter 3, *Speckle Metrology*, Academic Press, Inc. (London) LTD. 1978.

[35] Vorburger, T.V., Teaque, E.C., *Optical Techniques For On-Line Measurement Of Surface Topography*, Precision Engineering, Vol. 3, No. 2, pp. 61-83, April, 1981.

[36] Tay, C. J., Wang, S. H., Quan, C., Ng, C. K., *Surface Roughness Measurement Of Semi-Conductor Wafers Using A Modified Total Integrated Scattering Model*, Optik Vol.113, No. 7, pp. 317–321, 2002.

[37] Hariharan, P., *Optical Interferometry, The post-Michelson era*, Australian Journal of Physics, Vol. 46, No. 1, pp. 103, 1993.

[38] Born, M., Wolf, E., *Principles of Optics*, seventh ed., Cambridge University Press, Cambridge, England, pp. 478, 1999.

[39] Stover, J. C., Chapter1-3, *Optical Scattering Measurement And Analysis*, McGraw-Hill, Inc. 1990.

[40] Amiri, M. and Tavassoly, M. T., *Fresnel Diffraction From 1D And 2D Phase Steps In Reflection And Transmission Modes*, Optical Communication 272, pp. 349–361, 2007.

[41] Duparre´, A., Ferre-Borrull, J., Gliech, S., Notni, G., Steinert, J., Bennett, J. M., *Surface Characterization Techniques For Determining The Root-Mean-*

Square Roughness And Power Spectral Densities Of Optical Components, Applied Optics Vol. 41, No. 1, pp. 154-171, January, 2002.

[42] Lascos, S.J., Cassidy, D.T., *Optical Phase And Intensity Modulation From A Rotating Optical Flat: Effect On Noise In Degree Of Polarization Measurements*, Applied Optics, Vol. 48, No. 9, pp. 1697-1704, 2009.

[43] Giacoletto, L. J., *Generalized Theory Of Multitone Amplitude And Frequency Modulation*, Proc. IRE 35, pp. 680–693, 1947.

[44] Francon, M., *Optical Interferometry*, Chapter VI, Academic press, New York and London, 1966.

[45] http://hyperphysics.phy-astr.gsu.edu/hbase/phyopt/michel.html

[46] http://www.nanoscience.com/education/afm.html

[47] http://www.colorado.edu/physics/phys5430/phys5430_sp01/PDF%20files/Michelson%20Interferometer.pdf

[48] http://www.ndt-ed.org/EducationResources/CommunityCollege/Ultrasonics/EquipmentTrans/piezotransducers.htm

Appendix A

Calculation for *PSD* of signal at detector

```
clear all;
A=1;
s=0;
theta=0;
f0=10000; %optical frequency
f1=50; %modulation frequency
hold on
for k=0:1:5
m=4*pi*170/633;
x=m;
%x=pi:0.6:m;
t = 0:0.001:0.6;
y1=BESSEL(k, x);
y2=A*y1*cos(2*pi*(f0+k*f1)*t+k*theta);
s=s+y2;
%x = sin(2*pi*50*t)+sin(2*pi*120*t);
%y = x + 2*randn(size(t));
Y = fft(s,512);
Py = Y.* conj(Y) / 512;
Pyy=10*log10(Py)
```

```
f = 1000*(0:256)/512;
plot(f,Pyy(1:257))
title('Frequency content of y')
xlabel('frequency (Hz)')
ylabel('power spectral density ')
end
Pyy1=Pyy';
save C:\TMP\powersp1.txt Pyy1 -ASCII –TABS
```

Appendix B

Calculation of Michelson interference with different step height

```
a1=0.5; % oringinal amplitude one arm(v)
a2=0.5; % oringinal amplitude one arm(v)
hold on
d=[0 0 0 0 0 0 80 80 80 80 80 80 157 157 157 157 157 157 230 230 230
230 230 230 316 316 316 316 316 316 390 390 390 390 390 390 470 470
470 470 470 470 550 550 550 550 550 550 632 632 632 632 632 632];
%for lamda=1500:0.1:1600;
lamda=632.8;
phi=4*pi*d*(lamda.^(-1)); % phase difference d is path length change
y=cos(phi);
yy=a1.^2+a2.^2+2*a1*a2*y;
plot ( yy);
%title(' Fresnel Intergral Calculation(incident angle is zero) ')
xlabel('position')
ylabel('normalized intensity')
```

Appendix C

Calculation for Michelson interferometer with step changing

```
clear all
a1=0.5; % oringinal amplitude one arm(mv)
a2=0.5; % oringinal amplitude one arm(mv)
hold on
lamda=633;
d=[0 10 20 30 40 50 60 70 80 230 240 250 260 270 280 290 300 310 320
330 340 350 360 370 380 390 400 410 420 430 440 450 460 470 480 490
500 510 520 530 540 550 560 570 580 590 600 610 620 630 633];
phi=4*pi*d*(lamda.^(-1)); % phase difference d is path length change
y=cos(phi);
yy=a1.^2+a2.^2+2*a1*a2*y;
plot (yy);
```

Appendix D

Sample preparation

1 Cleaning procedures for 2 inches Silicon wafer

- Clean one Pyrex beaker by deionized water and rinse with 10 mL H_2SO_4.
- Put 100 mL H_2O_2 and 50mL H_2SO_4 solution into the beaker and place the beaker on a heater until 80 ºC.
- Use a dipper to put the silicon wafer by into the beaker for 10 minutes.
- Lift the wafer out and dip into deionized after the wafer cooled for half minute.
- Rinse the wafer for 2 minutes and dry it by Nitrogen gas in the laminar flow unit. Do not leave any water on the wafer, which results in oxidation.
- For higher cleaning requirement, Teflon beaker will be used.
- Rinse a Teflon beaker and put 125 mL deionized water and 25 mL HF into the beaker.
- Dip wafer into the above solution for 2 minutes.
- Lift the wafer and dip into a beaker with deionized water for 5 minutes.
- Dry the wafer using Nitrogen gas gun. The dried wafer should not have any water on.

- For HF beaker, the cleaning work should be kept in a fume hood and the waste from HF should go to waste container.
- Bake the wafer at 100 ºC for 5 minutes.
- Place the wafer in a Petri dish on top of a back paper.
- Dip wafer into the above solution for 2 minutes.
- Lift the wafer and dip into a beaker with deionized water for 5 minutes.
- Dry the wafer using Nitrogen gas gun. The dried wafer should not have any water on.

2 Oxide layer deposition

- Heat the furnace to 1000 ºC.
- Blow the wafer by Nitrogen gas.
- Put the wafer on the first spot of the ladder using wafer tweezers to warm up the wafer. The better place and final place is in the middle of the ladder because the middle spot can deposit more uniform for the whole wafer.
- To get different step height, the deposition time need to be calculated in the calculator of the oxidation. A contrast or experimental data set can be achieved corresponding to different oxide growth. For example, to grow a 200 nm oxide, 31 minutes are needed. After 31 minutes, put out the ladder carefully and use tweezers to hold wafer until it cools

down to lower 30 ºC. An infrared thermometer will be used to check temperature of the wafer. Finally put the wafer back to the Petri dish.

10 nm	15 nm	170 nm	500 nm	600 nm
40 seconds	1 minutes	25 minutes	50 minutes	60 minutes

Table D-1 Oxidation for Si wafer at 1000^{o}C, 111 orientations, and wet growth

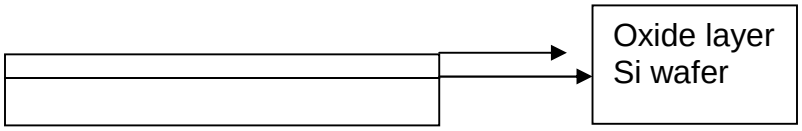

Figure D-1 Oxide layer on top of the Si wafer

3 Photo resist application on top of the wafer

- When photo resist are going to be applied, all light sources must be turn off, which will make photo resist exposed successfully.
- Turn on the power of the lamp in the fume hood and turn on the hot plate to 110 ºC for baking.
- Put three glass microscope slides one by one in the middle of the hot plate.
- Put the wafer support on the spinner and press it down and active the spinner for a while and stop it using the pedal.
- Dry or clean the wafer by Nitrogen gas gun and put it on the spinner and try to push the pedal to see if vacuum works properly.
- Set 4000 *RPM* to spin the spinner for 30 seconds.

- Withdraw photo resist using a 3 mL syringe, and from the middle of the wafer gently apply the photo resist one drop and one drop until the whole wafer is covered uniformly.
- Push the pedal to spin until it stops automatically.
- Remove the wafer-by-wafer tweezers and put it onto glass microscope slides on the hot plate, which should be 110 ºC.
- The soft baking time will last for 2 minutes.
- After soft baking, put the wafer into the Petri dish.

4 Pattern process

- UV exposure of photo resist is the key point of the whole processing, which will happen in the fume hood and laminar flow unit.
- Put the mask into the mask aligner after the pneumatics and electronics are all in working conditions.
- Place the wafer onto the wafer holder and make the wafer exactly parallel to the marker on the turntable, which is very important for later alignment.
- Push the turntable just under the mask, and then press the red button on the left to bring the wafer to the mask.
- This will give initial contact between them.
- After the initial alignment, use coarse alignment to adjust the wafer until both edges can get parallel.

- Set UV exposure time to 20 seconds.
- Push vacuum chamber and exposure button. It should be noted that one must avoid looking at the exposure when the buttons are pushed.
- After finishing the exposure, turn the red button back to loose the contact between the wafer and mask.
- Use wafer tweezers to put wafer back the Petri dish.
- After UV exposure, the development of the pattern needs to be done in a fume hood.
- Fill 200 mL developer solution (Micro posit 351) into a 500 mL Pyrex beaker.
- Fill 400 mL deionized water into another 500 mL beaker.
- Prepare a hot plate and set to 120 ºC and also put three glass microscope slides onto the hot plate.
- Dip the wafer into the developer solution and swirl for 40 seconds.
- Transfer the wafer and wafer tweezers into deionized water for 10 seconds and put the wafer onto a plate with flowing deionized water for 3 minutes.
- Move the wafer out and dry it by Nitrogen gas gun until no water is on.
- Gently put the wafer onto the hot plate.
- Hard baking time is for 2 minutes.
- Put the wafer back to the Petri dish.

- Dispose the waste into corresponding waste container and turn off the UV and hot plate.

5 SiO_2 layer etching

- Prepare a fume hood to do SiO_2 layer etching.
- Fill 200 mL buffered HF solution to a Teflon beaker.
- Prepare a 500 mL Pyrex beaker with 400 mL deionized water.
- Put the wafer into a Teflon dipper using wafer tweezers and place the dipper into the Buffered HF solution for several seconds to several minutes.
- The etching time depends on the step height that experiment needs.

10 nm	15 nm	200 nm	500 nm	600 nm
12 seconds	30 seconds	4 and half minutes	10 minutes	13 minutes

Table D-2 Timetable of Buffer HF etching for different step heights

- After Buffered HF etching, move the dipper into the beaker with deionized water and rinse 10 seconds.
- Using wafer tweezers to place the wafer into a plate with flowing deionized water for 3 minutes.
- Dry the wafer using Nitrogen gas gun and put it back to the Petri dish.

6 Photo resist removal

- Fill one beaker with 200 mL acetone (CH_3COCH_3) and one beak with 200 mL methanol (CH_3OH).
- Fill 400 mL deionized water into a 500 mL beaker.
- Put the wafer into acetone and swirl for 2 minutes.
- Transfer the dipper into methanol and swirl for a minute, and finally dip into the deionized water.
- After 3 minutes flowing deionized water rinsing, dry the wafer by Nitrogen gas gun and then put it back to the Petri dish.

7 Aluminum deposition

Aluminum layer deposition was performed by laboratory technician in the department of Engineering Physics at McMaster University. The wafer is located onto the deposition disk with front side down. Aluminum growth with 100 nm will be done in 15 minutes, and then use wafer tweezers to move the wafer back a Petri dish for measurement.